2021

Spectral properties of lunar impact melt deposits from Moon Mineralogy Mapper (M3) data

Catherine Neish
cneish@uwo.ca

Kevin Cannon
Colorado School of Mines

Livio Tornabene
Western University

Roberta Flemming
Western University

Michael Zanetti
NASA Marshall Space Flight Center

See next page for additional authors

Spectral properties of lunar impact melt deposits from Moon Mineralogy Mapper (M^3) data

C.D. Neish[1,2], K.M. Cannon[3], L.L. Tornabene[1,2], R.L. Flemming[1,2], M. Zanetti[4], E. Pilles[1,2]

[1]Department of Earth Sciences, The University of Western Ontario, London, ON, N6A 5B7 (cneish@uwo.ca)

[2]Institute for Earth and Space Exploration, The University of Western Ontario, London, ON, N6A 5B7

[3]Department of Geology and Geological Engineering, Colorado School of Mines, Golden, CO, 80401

[4]NASA Marshall Space Flight Center, Huntsville, AL, 35808

Paper accepted in Icarus

February 5, 2021

Abstract

Lunar impact melt deposits have unusual surface properties, unlike any measured terrestrial lava flow. Radar observations suggest that they are incredibly rough at decimeter scales, but they appear smooth in high-resolution, meter-scale optical images. The cause of their unusual surface roughness is unknown. In this work, we investigate the properties of impact melt deposits from seven lunar craters, ranging in size from 7.5 to 96 km in diameter, in an effort to understand the cause of their unique surface texture. We use data from the Lunar Reconnaissance Orbiter's (LRO) Mini-RF instrument to characterize the small-scale roughness of the deposits, data from the LRO Camera (LROC) to characterize their meter-scale morphology, and data from Chandrayaan-1's Moon Mineralogy Mapper (M^3) to characterize their composition. This represents the most comprehensive study of the composition of lunar melt deposits completed to date. In particular, we applied a customized spectral unmixing model to the M^3 data using laboratory spectra acquired from a range of possible lunar endmembers: pyroxene, olivine, fast-quenched lunar glass simulants, and impact melts and breccias (both synthetic and natural). We found that spectra derived from lunar melt deposits are typically modeled as a mix of the pyroxene and/or impact melts and breccias endmembers. Our modeled results suggest that lunar melt deposits are either crystalline deposits of pyroxene-rich rocks, or a mixture of glassy material and pyroxene minerals. The latter interpretation could explain the roughness observed in the Mini-RF data, if the melt deposits have a glassy surficial layer that shatters during impact gardening to produce decimeter scale blocks.

Key Words: Impact processes; Cratering; Moon; Moon, surface

1. Introduction

Deposits of smooth, low albedo material are observed around many fresh impact craters on the Moon [*Howard and Wilshire*, 1975; *Hawke and Head*, 1977; *Bray et al*., 2010; *Neish et al*., 2014; *Stopar et al*., 2014]. These deposits have been interpreted to be solidified melt from the impact event, ejected during the late stages of impact crater formation [*Hawke and Head*, 1977; *Osinski et al.*, 2011]. Different forms of the deposits have been observed, including ponds, veneers, and flows. In many cases, the morphologies of lunar impact melt flows appear very similar to the morphologies of lava flows [e.g., *Bray et al*., 2010; *Denevi et al*., 2012].

Despite their resemblance to lava flows in optical images, lunar impact melt deposits have a surface texture unlike any known terrestrial lava flow [*Neish et al*., 2017]. They are incredibly rough at decimeter scales, with radar returns at S-Band (12.6 cm) similar to blocky lava flows on Earth [*Campbell et al.*, 2010; *Carter et al*., 2012; *Neish et al.*, 2014; *Neish et al*., 2017]. However, in high-resolution optical images (~1 m scale), they appear quite smooth, more similar to pahoehoe flows than blocky flows (Figure 1) [*Bray et al*., 2010; *Neish et al*., 2017]. The reason for the unusual surface roughness of these flows is unknown.

One explanation is that the unique properties of lunar impact melt deposits relate to the thermal conditions under which they formed. The surface texture of

basaltic lavas, for example, are known to be strongly influenced by the efficiency of surface cooling [*Keszthelyi and Denlinger*, 1996]. The cooling conditions of lunar impact melt deposits differ markedly from terrestrial lava flows, which may explain the observed differences in their surface roughness. Lunar impact melt deposits cool under vacuum with initial temperatures often far in excess of their liquidus [*Simonds et al.*, 1976; *Timms et al.*, 2017], while terrestrial lava flows cool under a convective atmosphere with initial temperatures just above their liquidus. Lunar impact melts also incorporate clasts of broken rock from the impact event, which further alter their cooling conditions compared to terrestrial lava flows, and are composed of whole rock melt, rather than a partial melt [*Osinski et al.*, 2018].

At the decimeter scale (S-Band, 12.6 cm), impact melt deposits on Mercury show similar surface textures to those on the Moon in radar data [*Neish et al*., 2013], while impact melt flows on Venus do not [*Dong et al.*, 2015]. No impact melts have been studied on Mars using radar data, but the lava flows there are often exceptionally rough at the decimeter scale [*Harmon et al*., 2012]. Young lava flows on the Moon, in contrast, are often smooth at the decimeter scale [*Neish et al.*, 2017], although some older mare deposits have increased radar backscatter at this scale [*Campbell et al.*, 2009]. We thus posit that the unique cooling conditions experienced by lunar impact deposits (initially superheated, clast-choked, whole rock melt cooling under vacuum) may produce different

surface textures than those experienced by lava flows, or impact melts on worlds with thick, convective atmospheres.

In this work, we seek to characterize the physical and chemical properties of lunar impact melts in an effort to better understand the origin of their unusual surface texture. We use data from the Lunar Reconnaissance Orbiter's (LRO) Mini-RF instrument [*Nozette et al*., 2010] to characterize the decimeter-scale texture of the deposits, data from the LRO Narrow Angle Camera (LROC NAC) to characterize their meter-scale morphology [*Robinson et al*., 2010], and data from Chandrayaan-1's Moon Mineralogy Mapper (M^3) [*Pieters et al*., 2009] to characterize their composition. In particular, we look for evidence in the M^3 data for spectral signatures that are consistent with one of four lunar endmembers: pyroxenes (EM1), olivines (EM2), fast-quenched lunar glass simulants (EM3), and impact melts and breccias (both synthetic and natural) (EM4). We use laboratory spectra of these end members as inputs for the spectral unmixing model described in *Cannon et al*. [2017].

One hypothesis that we seek to test is whether the unique cooling conditions experienced by lunar impact melt deposits cause them to form with a glassy surficial layer. Glasses are typically more brittle than polycrystalline rocks, which means they will suddenly fail by breaking into smaller pieces with no deformation [*Altindag*, 2010]. Rocks with higher mechanical strength are more brittle than those with low mechanical strength, and obsidian has a compressive

109 strength twice that of basalt [*Fullagar and Torrence*, 1991, *Kahraman et al.*,
110 2018]. We thus speculate that a glass-rich layer on a lunar melt deposit will be
111 disrupted after formation to produce decimeter sized blocks covering an otherwise
112 'smooth' flow, similar to experiments conducted with melted basalt at the
113 Syracuse University Lava Project (Figure 2). These experiments – which heat 800
114 pounds of crushed Wisconsin basalt to 1200°C for several hours – typically
115 produce smooth, glassy lava flows [*Karson and Wysocki*, 2012]. On the Moon,
116 impact melt deposits may be disrupted as a consequence of small impacts
117 breaking apart the surface crust [*Ashworth,* 1978], or the result of the explosive
118 degassing of volatiles trapped in the melt during cooling of the impact melt
119 deposit [*Zanetti et al*., 2011]. Note that radar has a penetration depth of up to 10
120 times the illuminating wavelength on the Moon [*Neish et al*., 2011], so these
121 blocks could be buried by up to a meter of regolith.

122 Evidence of glass in impact melt deposits is found in both returned
123 samples and remote sensing data of the lunar surface. Lunar impact melt breccias
124 often show a mixture of both crystalline and glassy material [e.g., *Daubar et al*.,
125 2002, *Tompkins and Pieters*, 2010], and there are rare examples of glassy impact
126 melt rocks in the Apollo collection [*Osinski et al.*, 2018]. For example, sample
127 64455 from the Apollo 16 collection is an egg-shaped object almost completely
128 covered with black glass [*Ryder and Norman*, 1980]. Spectral evidence for glass
129 in and around lunar impact craters has also been noted in a number of previous

studies [*Smrekar and Pieters*, 1985; *Mustard et al.*, 2011; *Dhingra et al.*, 2013; *Horgan et al.*, 2014]. This evidence of glass is bolstered by the identification of volcanic glasses using similar data sets and methods [e.g., *Besse et al.*, 2014; *Cannon et al.*, 2017]. However, no comprehensive survey of the spectral properties of melt-bearing craters has yet been undertaken. We aim to complete such a survey in this work.

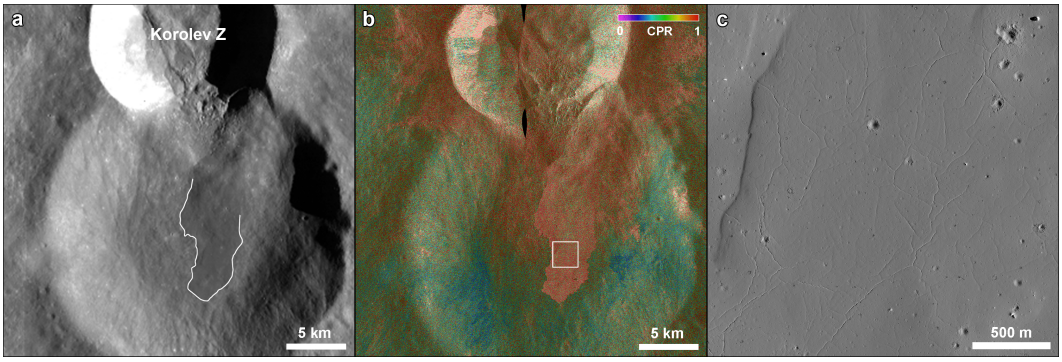

Figure 1: (a) A large melt deposit, outlined in white, is observed to flow out of the southern rim of Korolev Z in this LROC WAC mosaic. (b) The Mini-RF data indicate that this flow is blocky at the decimeter scale, yet a (c) close-up view of the melt flow and roughness analyses conducted by *Neish et al.* [2017] suggest it is smooth at the meter scale (LROC image M145671603RE.IMG). The location of (c) is shown by a white box in (b).

Figure 2: (a) A smooth but glassy flow produced at the Syracuse University Lava Project (http://lavaproject.syr.edu) by pouring melted basalt over sand under the terrestrial atmosphere. (b) When later broken apart, the flow fragments into centimeter- to decimeter-sized blocks with sharp edges. A quarter is seen at top left for scale. Image credit: Catherine Neish.

2. Methods

2.1 Laboratory spectra

Laboratory spectra of both synthetic and natural lunar materials were acquired for comparison to spectra of impact melt deposits on the Moon. The synthetic samples were of two different compositions: highlands-like and mare-like. They were melted, then quenched in two different ways for a total of four

160 samples (Figure 3). The materials were synthesized from raw oxide and carbonate
161 powders using the same methods described in detail by *Cannon et al.* [2017], one
162 with an average lunar highlands composition and one an average mare
163 composition [*Taylor and McLennan*, 2009]. The resultant spectra were obtained at
164 the Reflectance Experiment Laboratory (RELAB) facility (drop-quenched), and
165 using an ASD FieldSpec Spectrophotometer (slow-quenched).

166 As described in *Cannon et al.* [2017], drop-quenched samples were
167 measured with the custom-built UV-VIS-NIR bidirectional reflectance
168 spectrometer in the NASA RELAB facility at Brown University [*Pieters*, 1983].
169 The measured reflectance spectra cover 300 – 2550 nm with a sampling interval
170 of 10 nm, and pressed halon was used as a white reference to achieve absolute
171 reflectance values. Incidence and emergence angles were 30 and 0 degrees,
172 respectively. Because the RELAB detector was undergoing extensive
173 maintenance at the time the experiments were conducted, we measured slow-
174 quenched VNIR spectra using an ASD FieldSpec Spectrophotometer.
175 Measurements were made using an ASD light source oriented at 30 degrees, and
176 the fiber optic oriented vertically above the sample (i.e., 0 degrees). Details about
177 the quenching procedures are given below.

178 First, we used spectra from a previous set of experiments [*Cannon et al.*,
179 2017] of pure quenched glass samples, which lacked any signs of crystallization
180 detectable to the unaided eye. These experiments used a platinum loop technique

in a vertical 1 atm gas mixing furnace held at an oxygen fugacity (f_{O2}) of 1.5 log units below the iron-wüstite (IW) solid oxygen buffer, similar to lunar conditions [*Sutton et al.*, 2005]. Here, beads of melt were dropped from the hot spot of the furnace into a beaker of water, cooling from above the liquidus to ambient temperature in less than 1 second. These cooling rates are analogous to lunar pyroclastic glasses [*Hui et al*., 2018], which are formed from fine droplets of melt explosively launched into a vacuum. This method produced quenched glasses with broad one and two micron bands, and these broad features are similar to but distinguishable from crystalline pyroxene and/or olivine (based on their band centers; see Table 1 and Figure 4). These spectra are similar to the re-melted "prepared glass" spectra presented in *Tompkins and Pieters* [2010], which are chemically equivalent to their Apollo 17 impact melt samples.

New to this study, two slow-cooled synthetic melts were also prepared. We melted mixed powders (identical to the ones in the drop quench experiments) in 2 ml alumina crucibles in a horizontal 1 atm gas mixing furnace ($\log(f_{O2}) = -1.5$). Quenching was accomplished by shutting off the power to the furnace, such that the melt cooled from above the liquidus to ambient temperatures at a relatively fast rate (on the order of hours), but much slower than the quenched melts described above. Throughout, we refer to these as "slow-cooled" or "synthetic" melts, and they are somewhat analogous to the cooling conditions experienced by a melt flow emplaced onto the lunar surface (although not under

vacuum, nor of the volume expected for a melt flow). Upon visual inspection, this form of quenching produced an opaque material with no clear signs of crystallization for the mare composition, but showed clear evidence of crystallization for the highlands composition (Figure 3). The spectral signature of the highlands material at visible/near-infrared (VNIR) wavelengths shows broad one- and two-micron absorption bands (the band centers are at 0.99 μm and 2.19 μm; see Table 1 and Figure 4), possibly from the presence of pyroxene. The slow-cooled mare material is comparatively darker and has much lower spectral contrast, with muted one and two micron absorption bands (with band centers at 1.27 μm and 1.95 μm).

To confirm the presence of crystallites in the slow quenched samples and to determine their mineralogy, the highlands and mare samples were analyzed using microXRD (X-ray diffraction). X-ray diffraction is a technique by which a crystal lattice structure is inferred from the interaction of incident X-rays with the sample, producing constructive interference when conditions satisfy Bragg's law [*Klug and Alexander*, 1962]. The crushed, coarsely-crystalline samples were mounted on an oriented quartz holder and placed on a Bruker D8 Discover micro X-ray diffractometer using Co Kα radiation ($\lambda_{Co\ K\alpha 1}$ = 1.78897 Å) (see *Flemming* [2007] for geometry). They were then oscillated over 2 mm to allow the nominal 300-micron X-ray beam to sample more of the crystallites. Both samples showed evidence for multiple crystalline minerals. An automated search using the

223 International Centre for Diffraction Data (ICDD) PDF2 database revealed the
224 presence of plagioclase (anorthite) in both the highlands and mare samples, with
225 additional evidence for small amounts of olivine (forsterite) (Figure 5).
226 Clinopyroxene (augite) could also be present, however, its identification is not
227 definitive due to considerable peak overlap with anorthite (see Figure 5 and the
228 discussion below). In addition, an iron alloy was identified in the mare sample, as
229 well as a small amount of ilmenite.

230 Although the VNIR spectra of the slow quenched highlands melt strongly
231 suggests the presence of pyroxene, the XRD results suggest there is comparatively
232 little pyroxene in the sample. However, previous work has demonstrated that
233 small amounts of pyroxene (2-10%) can dominate the VNIR spectral signature
234 when mixed with spectrally "bland" materials like glass or plagioclase [*Tompkins*
235 *and Pieters*, 2010; *Cheek and Pieters*, 2014]. Pyroxene should be detectable by
236 XRD down to ~1% [*Hill et al.,* 1993], using specialized methods like Rietveld
237 modal analysis. Unfortunately, our dataset was not amenable to Rietveld
238 refinement, so we performed conventional interpretation by visual inspection
239 using the ICDD database. This database cannot definitively identify low-
240 symmetry phases with modal proportion <5% due to peak overlap [*Klug and*
241 *Alexander*, 1962]. Given the considerable peak overlap between the low-
242 symmetry phases anorthite (triclinic) and pyroxene (monoclinic), in addition to
243 olivine (orthorhombic), we estimate that there could be 5-10% pyroxene present

244 in this sample, as supported by VNIR data acquired of the same sample.

245 Finally, we used spectra of pure pyroxene and olivine samples from the
246 RELAB database, as well as spectra from actual Apollo impact melt and melt
247 breccia samples to compare to the spectra of impact melt deposits on the Moon
248 (Table 1). The Apollo samples that we used in this study are similar to other
249 impact melt and melt breccia samples for which spectra have been acquired
250 [*Tompkins and Pieters*, 2010]. This representative spectral library was used to
251 interpret the remote sensing data described in Section 2.2. These spectra are
252 unique from one another, allowing us to distinguish quenched glasses from pure
253 mafic minerals (pyroxene and olivine) as well as from materials with a mixture of
254 glass and crystals (synthetic slow-cooled melts, Apollo melts and melt breccias).
255 However, geologic context is necessary to properly interpret the results. For
256 example, quenched glasses are also found in pyroclastic deposits, while minerals
257 in partially crystallized and/or clast-bearing impact melts (pyroxene, olivine,
258 plagioclase) may be found in extrusive or intrusive igneous rocks.

259 All of the spectra used in this work were continuum removed using the
260 "Continuum Removal" function available in ENVI 5.5, over the wavelength range
261 of 0.5 to 2.5 microns. In short, the continuum is removed by dividing the original
262 spectrum by the continuum curve. The continuum curve is calculated by fitting a
263 convex hull over the top of the spectrum, using straight-line segments that
264 connect local maxima. *Besse et al.* [2011] found that the ENVI continuum

removal has some limitations when applied to noisy spectra, and could possibly shift the M^3 band centers. However, when we implemented a manual continuum removal for one representative spectrum, we found a shift in band position of only 10-20 nm. We have thus decided to utilize the ENVI continuum removal for this work. We then calculated the band centers for each spectrum by fitting an 11^{th}-order polynomial to the 1 and 2 micron bands, and determining the minimum of the fit to the absorption band. For the glass spectra, we had to remove a linear slope in the data before fitting the polynomial to the 2 micron band. The results are presented in Table 1.

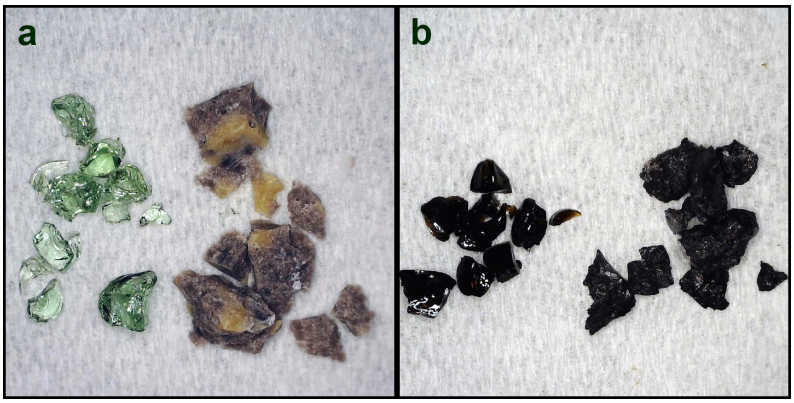

Figure 3: (a) Samples of melted highlands material that has been drop quenched (left) compared to identical melt that has also been quenched, but more slowly (right). (b) Samples of melted mare material that has been drop quenched (left) compared to identical melt that has also been quenched, but cooled more slowly (right). Although identical in composition, the differences in cooling rate produce solid samples that are visually and spectrally distinct from one another. In particular, the drop-quenched samples are distinctly more vitreous in luster, indicating that they are glassier than the slow-quenched samples.

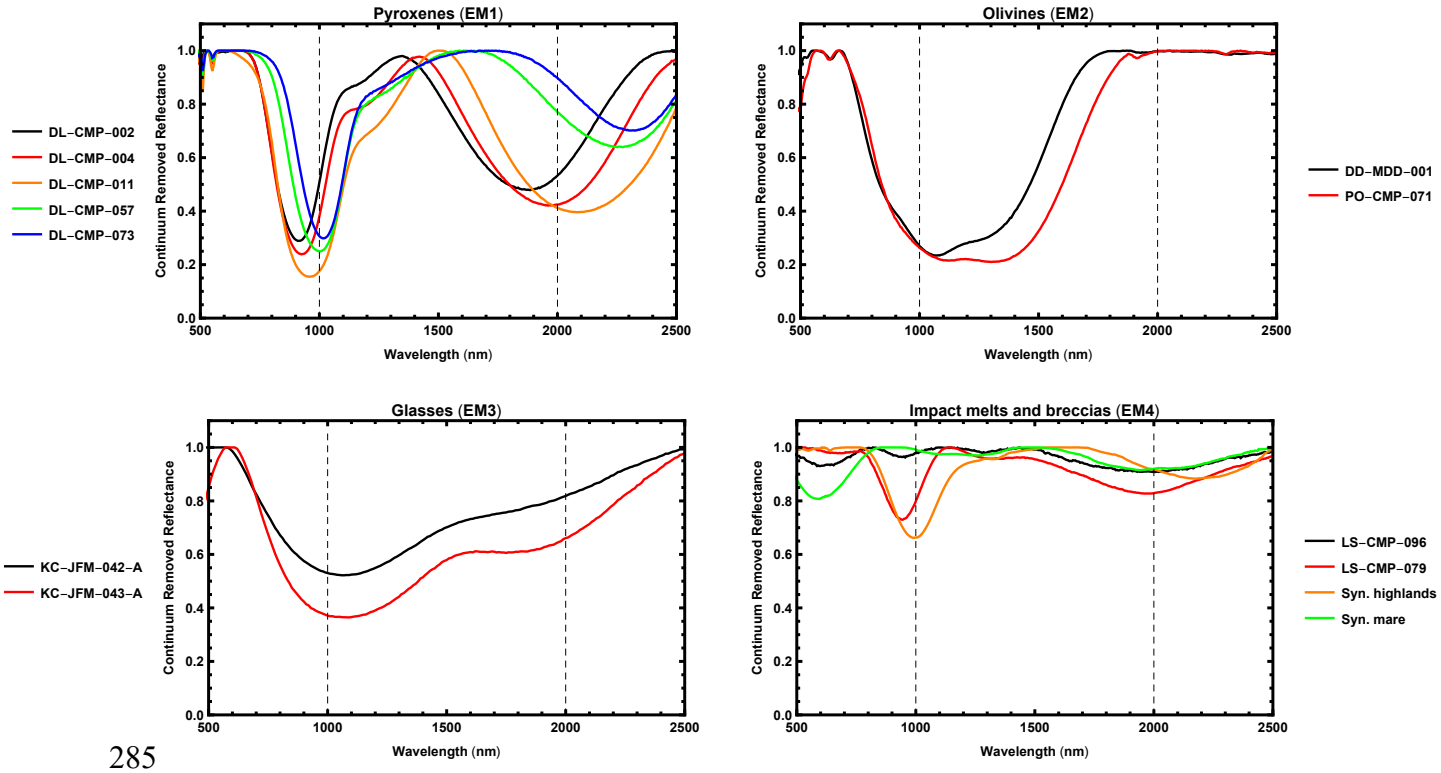

285

286 **Figure 4**: Continuum removed VNIR spectra of the four sets of lunar end
287 members studied in this work: pyroxenes (EM1), olivines (EM2), fast-quenched
288 lunar glass simulants (EM3), and impact melts and breccias (both synthetic and
289 natural) (EM4). A description of each spectrum is given in Table 1. Note that the
290 fast-quenched glass samples are low contrast and show shallow, broad absorption
291 bands centered near one and two microns, while the slow-quenched, synthetic
292 highlands melt shows more distinct absorption bands, consistent with the presence
293 of crystalline pyroxene (it appears most similar to the synthetic clinopyroxene
294 $Wo_{25}En_{36}Fs_{39}$, DL-CMP-057).
295

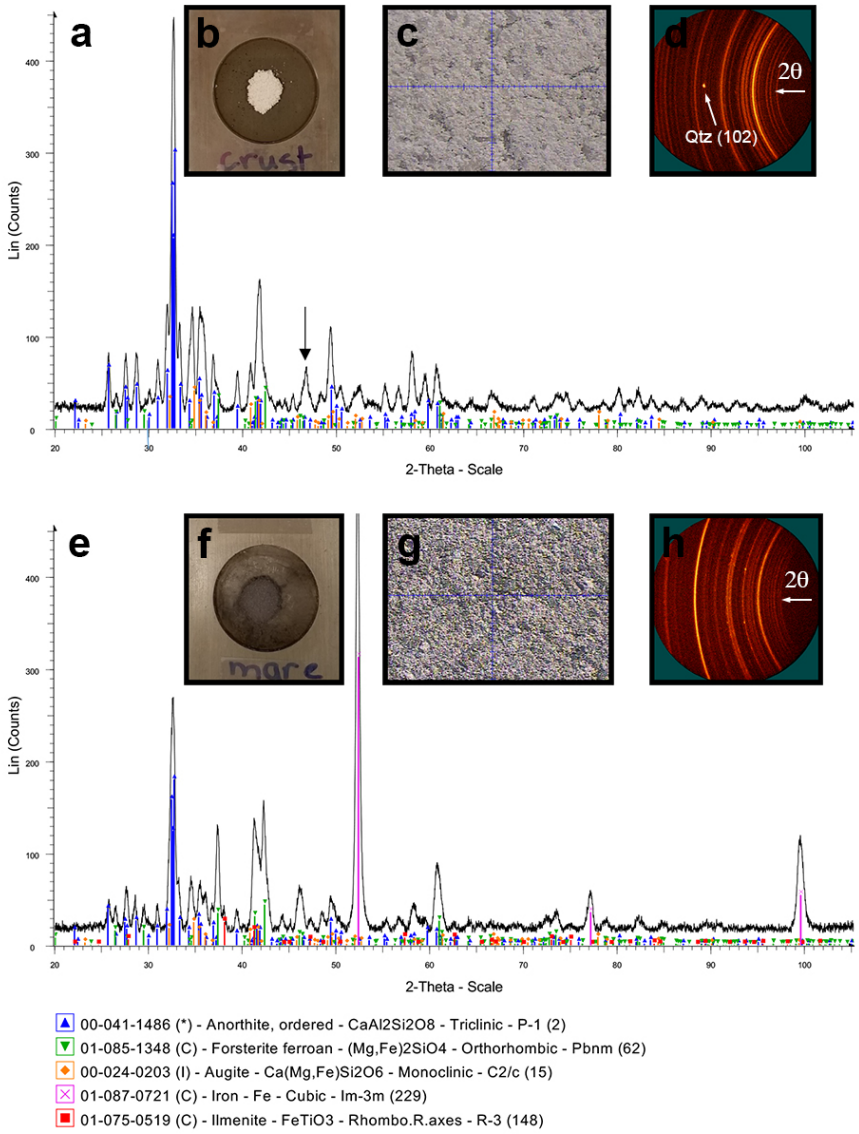

Figure 5: XRD results for the slow-quenched (a) highlands and (e) mare samples. Diffraction patterns show that anorthite (blue), forsterite (green), and clinopyroxene (orange) were identified in both samples. An iron alloy (pink) and ilmenite (red) were identified in the mare sample. (b and f) Highlands and mare samples are shown mounted on a one inch diameter oriented quartz sample holder. (c and g) Highland and mare target locations, as viewed through the microscope on the XRD (FOV = 2 mm). Shards of glass can be seen in the highlands sample in image (c). A variety of colours and textures can be seen in image (g), visibly indicating multiple phases. (d and f) Two-dimensional General

306 Area Detector Diffraction System (GADDS) images for highlands and mare
307 samples. Homogenous Debye rings in (d) indicate fine-grained material (<5 μm).
308 Grainy or 'spotty' rings in (h) are indicative of some phases having courser grain
309 sizes (>10 μm). The bright spot in d (black arrow in a) is due to a signal from the
310 quartz sample holder. Instrumental parameters are as follows: coupled scan, two
311 frames (θ1 = θ2 = 20°), width between frames = 45°, time = 2 hr/frame. The
312 sample was oscillated 2 mm in XY during data collection. Each conventional
313 intensity versus 2-Theta diffraction pattern shown here has been derived by
314 integration of two GADDS images, with subsequent background subtraction and
315 phase identification using the ICDD PDF2 database.
316
317 **Table 1**: Description of spectra used for the four endmembers in the spectral
318 unmixing model.

Pyroxenes (EM1)	**RELAB ID**	**Band Centers (μm)**
Synthetic orthopyroxene $Wo_0En_{80}Fs_{20}$	DL-CMP-002[a]	0.91, 1.88
Synthetic orthopyroxene $Wo_0En_{50}Fs_{50}$	DL-CMP-004[a]	0.93, 1.97
Synthetic pigeonite $Wo_{14}En_{36}Fs_{50}$	DL-CMP-011[a]	0.96, 2.09
Synthetic clinopyroxene $Wo_{25}En_{36}Fs_{39}$	DL-CMP-057[a]	1.00, 2.26
Synthetic clinopyroxene $Wo_{39}En_{36}Fs_{25}$	DL-CMP-073[a]	1.02, 2.31
Olivines (EM2)		
Olivine from Chassigny Fo_{68}	DD-MDD-001	1.09, N/A
St. Peter's Fayalite	PO-CMP-071	1.29, N/A
Glasses (EM3)		
Fast-quenched synthetic highlands glass	KC-JFM-042-A[b]	1.07, 1.98
Fast-quenched synthetic mare glass	KC-JFM-043-A[b]	1.07, 1.99
Impact melts and breccias (EM4)		
Slow-quenched synthetic highlands melt	N/A[c]	0.99, 2.19
Slow-quenched synthetic mare melt	N/A[c]	1.27, 1.95
Apollo 15 impact melt 15445,261	LS-CMP-096-D[d]	0.94, 1.98
Apollo 17 impact melt breccia 76295,123	LS-CMP-079[d]	0.94, 1.97

319
320 [a]Described by *Klima et al.* [2011].
321 [b]Described by *Cannon et al*. [2017].
322 [c]These are new spectra acquired in this work. They are available in the Supplementary
323 Material.
324 [d]Described by *Tompkins and Pieters* [2010].
325

326 *2.2 Remote sensing data sets*

327

328 In this work, we used Moon Mineralogy Mapper (M^3) data to constrain the
329 mineralogy of seven representative lunar craters with deposits of impact melt
330 (Table 2). M^3 was a hyperspectral imager that collected data from 540 to 2976
331 nm, with a spectral resolution of 40 nm and a spatial resolution of 140 m/pixel in
332 the global imaging mode [*Pieters et al.*, 2009]. For each crater, we identified one
333 or more M^3 images with overlapping coverage of the crater. Where possible, we
334 selected images from Optical Period 1A, 1B, or 2A. During this period,
335 Chandrayaan-1 was in a lower orbit with a single star tracker intact; after this
336 period, Chandrayaan-1 was moved to a higher orbit (200 km vs. 100 km) and had
337 no working star trackers [*Green et al*., 2011]. As a result, the spatial resolution
338 was reduced to 280 m/pixel in Optical Periods 2B and 2C. In all cases, we used
339 the Level 2 reflectance (RFL) data for further analysis, and the corresponding
340 location (LOC) file for map projection. The Level 2 data have been thermally and
341 photometrically corrected as described in *Clark et al.* [2011] and *Besse et al.*
342 [2013], respectively. Although impact melts deposits are more common amongst
343 highlands craters [*Neish et al.*, 2014; *Stopar et al*., 2014], craters were selected to
344 represent a mix of both highlands and mare target materials. All selected craters
345 display prominent impact melt deposits (i.e., ponds and flows) on their ejecta
346 blankets [*Neish et al.*, 2014]. We also avoided craters north or south of ~40°

347 latitude, as illumination geometry can influence the spectral parameter maps.

348 After cropping the M^3 data to the region of interest, we applied the
349 spectral unmixing model developed by *Cannon and Mustard* [2015] and
350 described in detail by *Cannon et al.* [2017] to the data over the spectral range 620
351 to 2597 nm. Briefly, this model uses linear unmixing in single-scattering albedo
352 space to represent a remote spectrum as a combination of laboratory and scene-
353 derived (i.e., from the M^3 data itself) endmembers. The scene-derived
354 endmembers were extracted by using the average of the detector column for each
355 pixel. A statistical F-test is used to evaluate whether a particular endmember of
356 interest (for example, EM3, fast-quenched lunar glass simulants) is likely to be
357 present in the remote spectrum, or if the remote spectrum can be well-modeled by
358 crystalline minerals (pyroxene/olivine) and neutral components alone.

359 The model is run on the original spectra, which have not been continuum-
360 removed, and iteratively compares these endmembers to find which has the lowest
361 F value. If the endmembers don't improve the model fit with statistical
362 significance, they are not modeled. For example, if a spectral feature is ubiquitous
363 and part of the "background" of the entire scene, then the model may not pick it
364 out as being distinct because it uses spectra from the scene itself as an
365 endmember. The model reports the fraction of each spectrum used in the fit in the
366 raw output. However, we chose not to report this information in the present work,
367 as our goal is not to identify the presence of a specific mineral, but rather to see if

368 we can distinguish melt deposits from mafic minerals. Instead, the results are
369 provided in a four-band image cube, where the individual bands are representative
370 of the input endmembers. These can be used to make RGB composite images to
371 provide a semi-quantitative representation of the different endmember mixtures
372 present at any point on the lunar surface.

373 The model is specifically designed to minimize false positive detections of
374 spectrally subtle materials like glasses, and does not attempt to derive absolute
375 physical abundances for the endmembers because of the highly non-unique
376 inversions involved. Nonetheless, any regions that are spectrally bland, with
377 broad but weak one and two micron bands, are difficult to confidently assign to an
378 endmember. Thus in some cases, there are false positive results where the spectral
379 model attempted to assign an endmember to a region that does not show distinct
380 spectral features. In previous work [*Cannon et al*., 2017], this model successfully
381 identified pyroclastic glass deposits in Alphonsus crater using M^3 data (i.e., the
382 fractional abundance was greater than zero), and was able to show that signatures
383 of glass decreased radially away from the volcanic vents.

384 We then map projected the resulting model outputs for all localities listed
385 in Table 2, and georegistered them to images from the Lunar Reconnaissance
386 Orbiter (LRO) Wide Angle Camera (WAC) and Narrow Angle Camera (NAC), as
387 well as radar images from the Mini-RF radar on LRO and from the Arecibo
388 Observatory (both at S-Band, 12.6 cm). Radar is sensitive to roughness at the

scale of the radar wavelength [*Neish and Carter*, 2014], so these maps provide information about the decimeter-scale roughness at the surface and near-subsurface (up to ~1 m in regolith). Using the optical and radar images, we mapped out obvious regions of melt for comparison to the spectral unmixing model. We produced two RGB composite images of the spectral unmixing results. In the first, the total crystalline mafic endmembers (pyroxenes, EM1, plus olivines, EM2) inferred from the model is represented by red, impact melts and melt breccias (EM4) by green, and pure quenched glasses (EM3) by blue. In the second, the total "impactite" content (fast-quenched lunar glass simulants, EM3, and impact melts and breccias, EM4) inferred by the model is represented by red, pyroxenes (EM1) by green, and olivines (EM2) by blue. We discuss each crater separately in Section 3.

Table 2: Craters investigated in this work, with corresponding M^3 data, in order of size.

Crater	Diameter (km)	Lat. (°N)	Lon. (°E)	Location	M^3 Image(s)	Spatial Resolution	Optical Period
Donner M	7.5	-32.2	97.9	Highlands	M3G20090601T062753_V01_RFL.IMG	280 m/pixel	2C
Tharp	13	-30.9	145.5	Highlands	M3G20090528T130108_V01_RFL.IMG	280 m/pixel	2C
Giordano Bruno	22	35.9	102.8	Highlands	M3G20090531T215442_V01_RFL.IMG	280 m/pixel	2C
Aristarchus	42	23.7	-47.3	Mare	M3G20090209T054031_V01_RFL.IMG M3G20090209T072710_V01_RFL.IMG	140 m/pixel	1B
Glushko	43	8.4	-77.6	Highlands/ mare border	M3G20090614T131003_V01_RFL.IMG	280 m/pixel	2C
King	76	5.0	120.5	Highlands	M3G20081231T034148_V01_RFL.IMG	140 m/pixel	1A
Copernicus	96	9.6	-20.1	Mare	M3G20090207T044515_V01_RFL.IMG	140 m/pixel	1B

403 **3. Results**
404

405 *3.1 Donner M*

406

407 Donner M is a ~7.5 km diameter crater located on the southern rim of
408 Donner crater. A prominent, lobate flow is seen emerging from the northern rim
409 of Donner M crater onto the floor of the more ancient Donner crater. Cooling
410 cracks and leveed channels are observed in the LROC NAC images, indicative of
411 its origin as an impact melt deposit [*Neish et al*., 2014]. The melt flow has high
412 radar backscatter and circular polarization ratios in the Mini-RF data set,
413 suggesting a surface that is blocky at the decimeter scale.

414 When the spectral unmixing model is applied to the M^3 data in this region,
415 the melt flow is mapped as a pyroxene deposit (Figure 6). The averaged spectrum
416 taken of this region shows the most similarities to the clinopyroxene spectrum
417 DL-CMP-011 given in Figure 7 (with band centers at 0.96 and 2.11 μm,
418 compared to 0.96 and 2.09 μm). In a large melt flow produced from a
419 predominately anorthositic target rock, we would expect pyroxene to form as part
420 of the crystallization sequence [*Vaughan et al*., 2013]. However, this does not
421 necessarily imply that the flow is a purely crystalline pyroxene exposure. Only a
422 small percentage of crystals are needed to show spectral evidence for pyroxene;
423 *Tompkins and Pieters* [2010] found that > 60% glass is necessary for the presence

of glass to be obvious in a mixed spectrum. Furthermore, *Cheek and Pieters* [2014] found that pyroxene is spectrally dominant at just 2 vol. % abundance in pyroxene-plagioclase mixtures. Therefore, even an intimate mixture dominated by plagioclase and/or glass may still not be spectrally distinct from the pyroxene endmember in our spectral unmixing model. (Note that the lunar highlands are dominated by anorthosite, so we would expect a large fraction of the melt to be plagioclase-rich [e.g., *Wānke et al*., 1975], even though it is readily masked by other phases in the VNIR.)

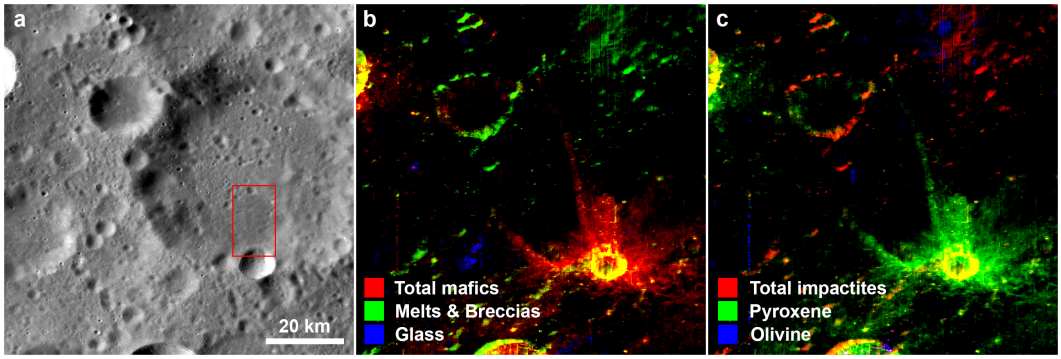

Figure 6: (a) LROC WAC mosaic of a small crater on the rim of Donner crater. The red box indicates the location of Figure 7. (b) Spectral unmixing results from the M^3 image M3G20090601T062753_V01_RFL.IMG. Here, red represents the combined mafic endmembers (pyroxenes, EM1, and olivines, EM2), green represents impact melt and breccia endmembers (EM4), and blue represents quenched glass endmembers (EM3). (c) Spectral unmixing results, where red represents the combined impactite endmembers (quenched glass, EM3, and impact melts and breccias, EM4), green represents pyroxene-rich endmembers (EM1), and blue represents olivine-rich endmembers (EM2). The red and blue bands in (b) and the green and blue bands in (c) have been scaled linearly from 0.01 to their maximum value, to remove spuriously low values. The green band in (b) and the red band in (c) have been scaled linearly from 0.1 to their maximum value.

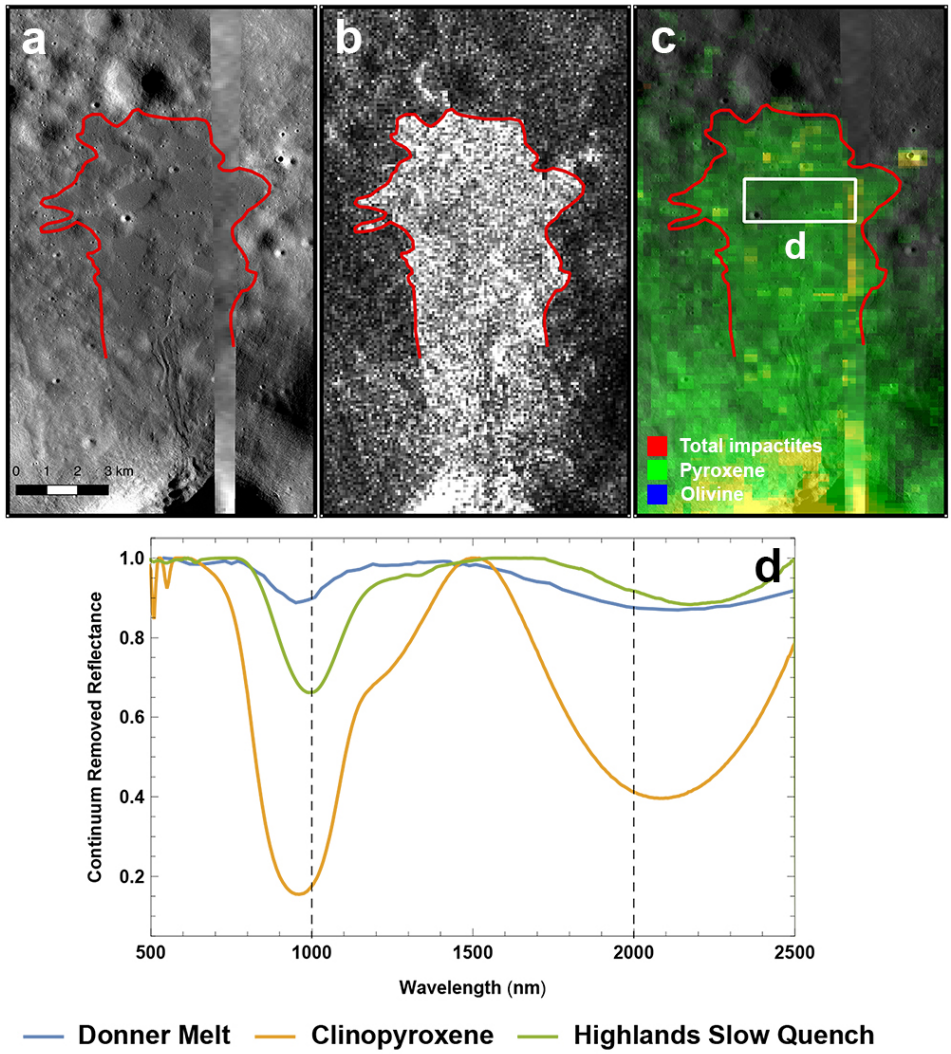

Figure 7: (a) LROC NAC mosaic of a prominent melt flow emanating from the northern rim of Donner M (M115672963.IMG, M131005361RE.IMG). The lobate portion of the flow has been outlined in red. (b) Mini-RF total power image of the same region indicates the melt flow is rough at the decimeter scale (LSZ_04611_1CD_XKU_35S098_V1.IMG). (c) Spectral unmixing results of this region suggest the flow is spectrally consistent with the pyroxene endmember (EM1). A white box indicates the region where the spectrum shown in (d) was extracted. (d) Average continuum removed spectrum of a portion of the melt flow from Donner M, compared to a clinopyroxene spectrum (sample DL-CMP-011) and the highlands slow quench spectrum given in Figure 4.

460 *3.2 Tharp*

461

462 Tharp is a fresh, rayed 13.5 km diameter crater in the lunar highlands, with
463 extensive downrange melt flows identified by *Carter et al.* [2012]. These deposits
464 are darker-toned with respect to their surroundings, consistent with other lunar
465 melts, and also exhibit cooling cracks and evidence of ponding in low-lying local
466 topography. Lobate margins, flow features, and possible evidence of inflation are
467 observed in one prominent melt flow observed west-northwest of the crater. This
468 melt has high radar backscatter in the Mini-RF data, indicating a surface that is
469 rough at the decimeter scale [*Carter et al*., 2012; *Neish et al.*, 2014].

470 When the spectral unmixing model is applied to the M^3 data in this region,
471 the Tharp ejecta blanket appears most consistent with a mixture of mafic
472 components and impact melts/breccias (Figure 8). Zooming in on an individual
473 melt deposit, we see that the model identifies the unit as being most consistent
474 with impact melts/breccias (Figure 9). An average spectrum of this region shows
475 evidence of pyroxene absorptions, similar to our slow-cooled synthetic highlands
476 melt. The band centers of the melt deposit are at 0.95 and 2.14 μm, compared to
477 0.99 and 2.19 μm for the slow-cooled synthetic highlands melt.

478 However, the melts/breccias spectral unit also appears elsewhere in the
479 unmixing model, in regions where there is no obvious melt. For example, there is
480 a strong signature just east of the crater, in a region of blocky ejecta (Figure 10).

Here, the presence of non-pyroxene phases such as plagioclase may be influencing the spectral model, producing spurious results (since plagioclase is spectrally bland). In another nearby region, a melt veneer was classified as a mafic exposure, with a pyroxene-like spectrum (Figure 10d). As in the case of Donner M, the melt could be a mixture of spectrally featureless components such as glass or plagioclase with small amounts of pyroxene. Both regions northeast of the crater have spectra with nearly identical band centers, 0.94 and 2.11 μm for the ejecta and 0.95 and 2.11 μm for the veneer.

The melts/breccias spectral unit also extends throughout much of the northern portion of Figure 8, possibly the result of rayed ejecta emanating from Tharp. Tharp has an obvious ray pattern in optical images, indicating impact was from the southeast towards the northwest [*Neish et al*., 2014]. The crater rays are consistent with the melts/breccia endmember, giving confidence that our model can distinguish melt-rich ejected materials from other possible endmembers. However, an average spectrum taken from this region is distinct from the melt deposits, with muted spectral absorption bands, and a two micron band that is offset from the melt spectra (Figure 11). The band centers in this region are found at 0.91 and 2.19 μm, compared to 0.95 and 2.14 μm for the melt deposits. These are likely pyroxene signatures mixed with different minerals.

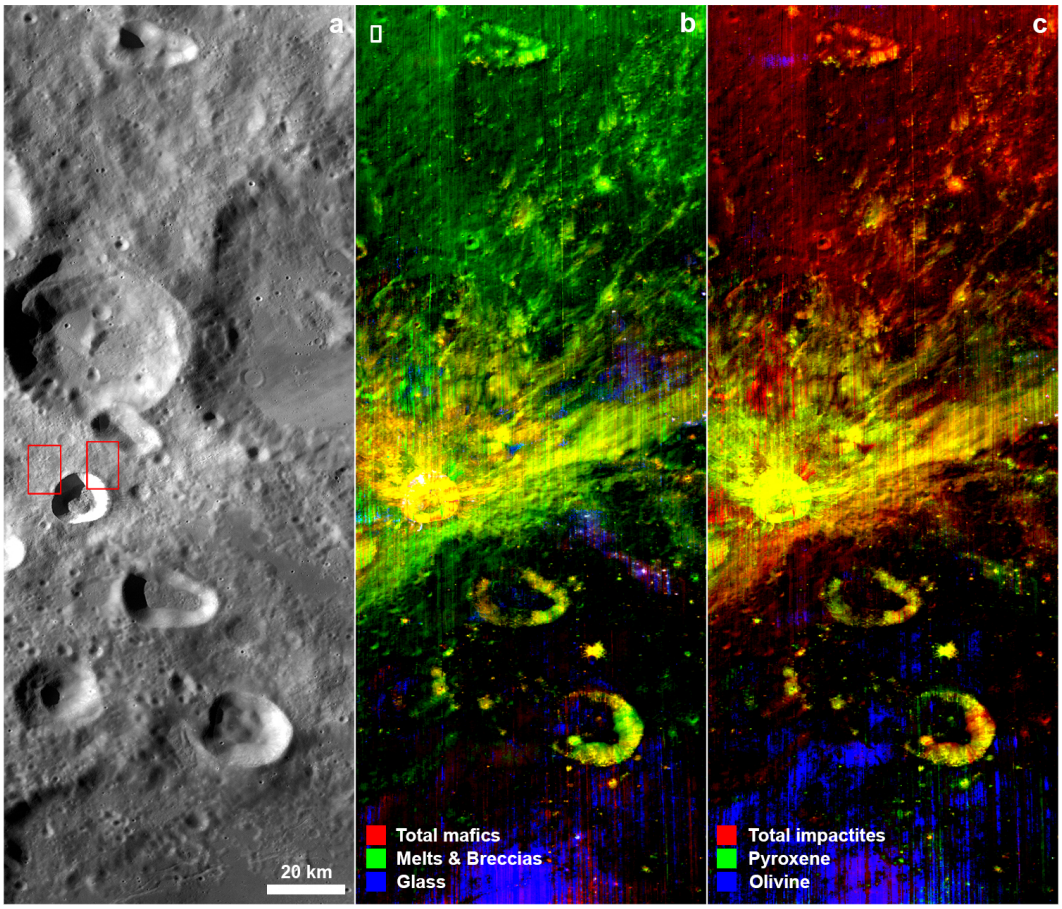

Figure 8: (a) LROC WAC mosaic of Tharp crater. The red boxes indicate the location of Figures 9 and 10. (b) Spectral unmixing results from the M^3 image M3G20090528T130108_V01_RFL.IMG. Here, red represents the combined mafic endmembers (pyroxenes, EM1, and olivines, EM2), green represents impact melt and breccia endmembers (EM4), and blue represents quenched glass endmembers (EM3). (c) Spectral unmixing results, where red represents the combined impactite endmembers (quenched glass, EM3, and impact melts and breccias, EM4), green represents pyroxene-rich endmembers (EM1), and blue represents olivine-rich endmembers (EM2). All bands have been scaled linearly from 0.01 to their maximum value, to remove spuriously low values.

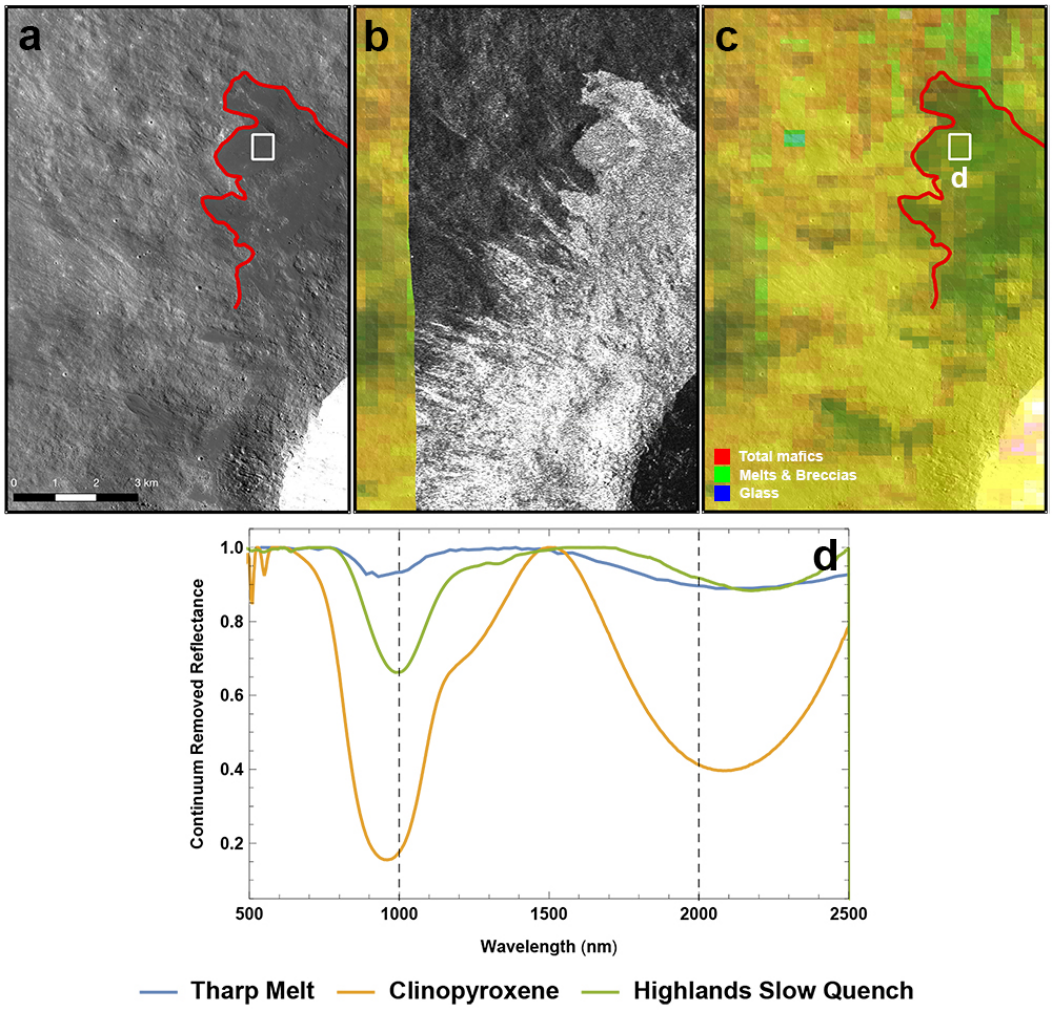

Figure 9: (a) LROC NAC image of a prominent melt flow emanating from the northwest rim of Tharp crater (M1107332576.IMG). The lobate portion of the flow has been outlined in red. (b) Mini-RF total power image of the same region indicates the melt deposit is rough at the decimeter scale (LSZ_02832_1CD_XKU_36S146_V1.IMG). (c) Spectral unmixing results of this region suggest the flow is consistent with the melt/breccia endmember (EM4). A white box indicates the region where the spectrum shown in (d) was extracted. (d) Average continuum removed spectrum of a portion of the melt flow from Tharp crater, compared to a clinopyroxene spectrum (sample DL-CMP-011) and the highlands slow quench spectrum given in Figure 4.

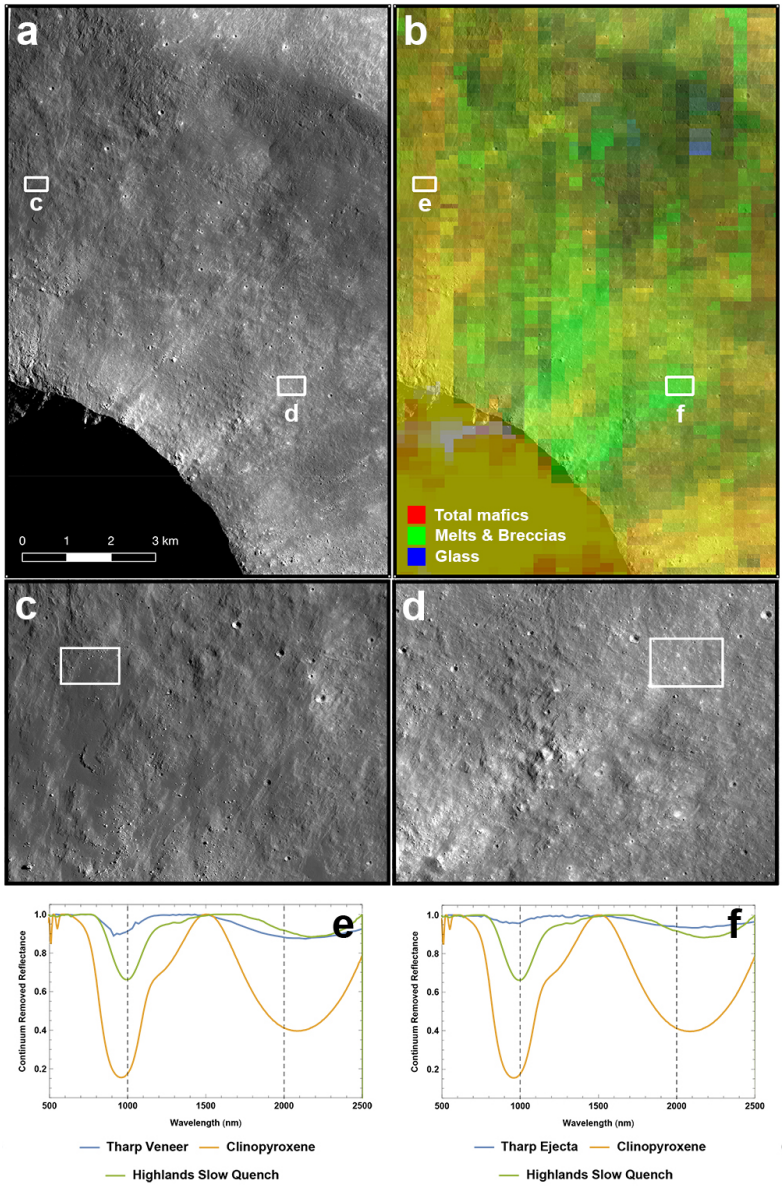

Figure 10: (a) LROC NAC image of ejecta emanating from the northeast rim of Tharp crater (M1183864794.IMG). White boxes indicate the regions shown in the close-ups in (c) and (d), where the spectra in (e) and (f) were extracted. (b) Spectral unmixing results of the region labeled (c) suggest the flow is consistent with mafics (EM1 + EM2), while the region labeled (d) appears consistent with melts/breccias (EM4). This is at odds with visual identification of a melt veneer in (c) and boulders in (d). (e, f) Average continuum removed spectra of two portions of the ejecta from Tharp crater, compared to a clinopyroxene spectrum (sample DL-CMP-011) and the highlands slow quench spectrum given in Figure 4.

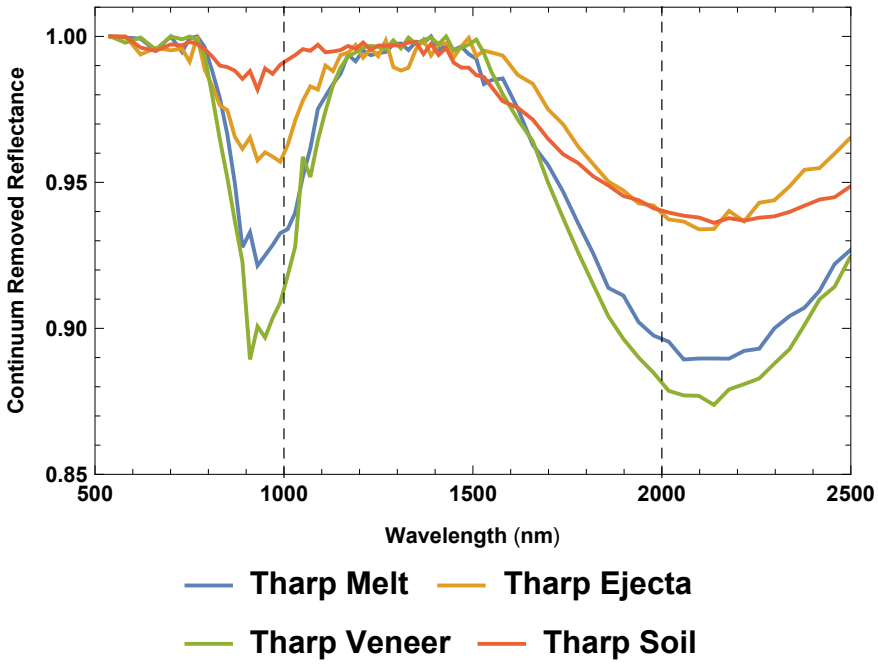

535

536 **Figure 11**: Average continuum removed spectra of four regions around Tharp
537 crater. Spectra were extracted from the white boxes given in the top left of Figure
538 8b (soil), Figure 9c (melt), Figure 10e and 10f (ejecta and veneer).
539

540

3.3 Giordano Bruno

Giordano Bruno is a fresh, rayed crater, and possibly the youngest large (D > 20 km) crater on the Moon. Crater counts suggest that it is 1–10 Ma [*Morota et al*., 2009], or even younger [*Plescia et al*., 2010]. High resolution observations of Giordano Bruno crater have revealed a wide variety of impact melt morphologies both interior and exterior to the crater rim. In particular, an extensive melt deposit is found south of the crater rim, which ends in an inflated flow margin [*Bray et al.*, 2010]. Recent spectral analysis of the crater found evidence for hydration features associated with the impact melt features at Giordano Bruno, which could be the result of both indigenous and non-indigenous sources of water [*Bhiravarasu et al.*, 2017].

When the spectral unmixing model is applied to the M^3 data in this region, the ejecta blanket appears to be quite diverse in composition (Figure 12). Portions of the ejecta appear consistent with pyroxene, while other areas (including a large region southeast of the crater) appear consistent with olivine. In terms of the melt deposits, the model identifies a prominent lobate melt flow south of the crater as being most consistent with mafics, predominantly pyroxene with some contributions from olivine (Figure 13). However, the spectral bands in this region are relatively weak and have broad absorption features near 1 and 2 μm, suggestive of pyroxene mixed with glass and/or other minerals. The band centers

562 in this region are found at 1.02 and 2.23 μm, compared to 1.00 and 2.26 μm for
563 the clinopyroxene DL-CMP-057 and 1.07 and 1.98 μm for the fast-quenched
564 highlands glass.

565 Melt flows and veneers also appear intermixed with the ejecta southeast of
566 the crater, in the region identified as olivine-bearing in the spectral unmixing
567 model (Figure 14). Again, the broad one-micron absorption features in this region
568 are relatively weak. It is therefore likely that the spectral model is interpreting a
569 broad one-micron band as olivine, but it is more likely another component,
570 possibly a mixture containing glass or low-contrast pyroxene. The band centers in
571 the SE1 region are found at 1.05 and 2.11 μm, while the band centers in the SE2
572 region are found at 1.04 and 2.17 μm. This can be compared to the band centers at
573 1.00 and 2.26 μm for the clinopyroxene DL-CMP-057, 1.09 μm for the olivine
574 DD-MDD-001, and 1.07 and 1.98 μm for the fast-quenched highlands glass. No
575 other surveys have identified olivine in this region [e.g., *Isaacson et al.*, 2011],
576 and it is typically exposed only in and around the rims of large impact basins
577 [*Yamamoto et al*., 2010].
578

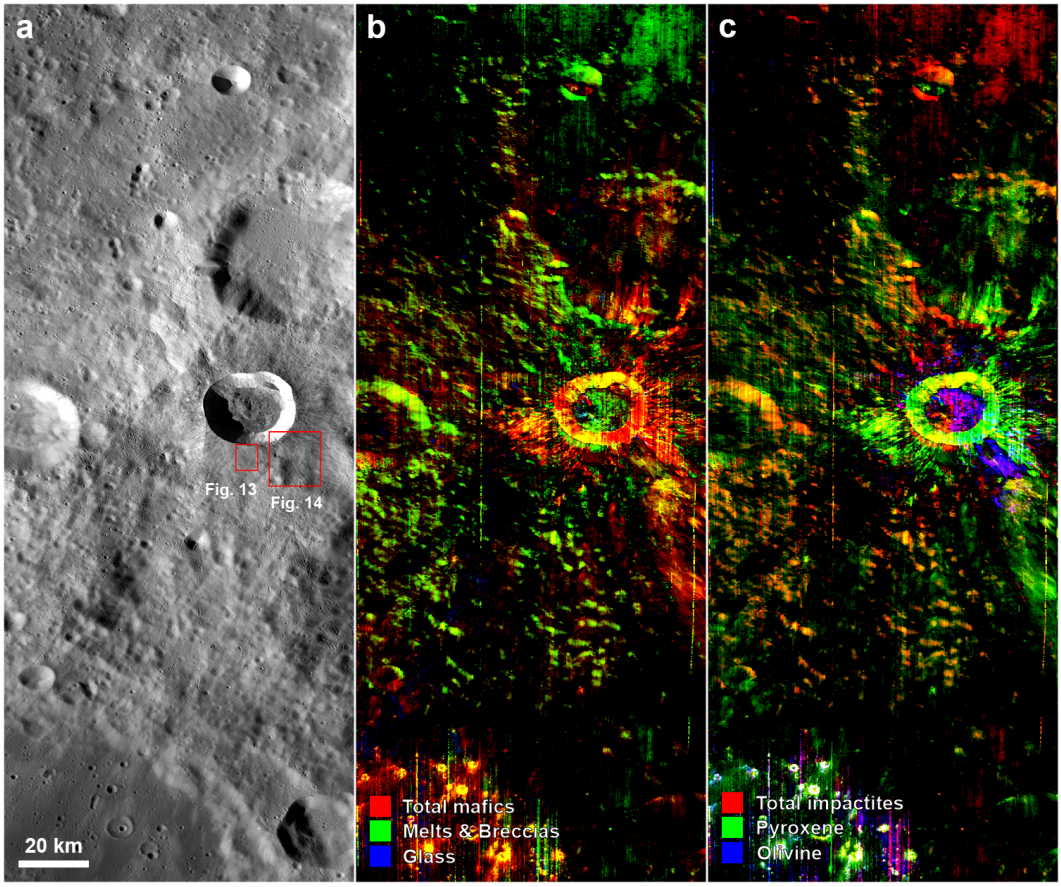

Figure 12: (a) LROC WAC mosaic of Giordano Bruno crater. The red boxes indicate the location of Figures 13 and 14. (b) Spectral unmixing results from the M^3 image M3G20090531T215442_V01_RFL.IMG. Here, red represents the combined mafic endmembers (pyroxenes, EM1, and olivines, EM2), green represents impact melt and breccia endmembers (EM4), and blue represents quenched glass endmembers (EM3). (c) Spectral unmixing results, where red represents the combined impactite endmembers (quenched glass, EM3, and impact melts and breccias, EM4), green represents pyroxene-rich endmembers (EM1), and blue represents olivine-rich endmembers (EM2). The red and blue bands in (b) and the green and blue bands in (c) have been scaled linearly from 0.01 to their maximum value, to remove spuriously low values. The green band in (b) and the red band in (c) have been scaled linearly from 0.1 to their maximum value.

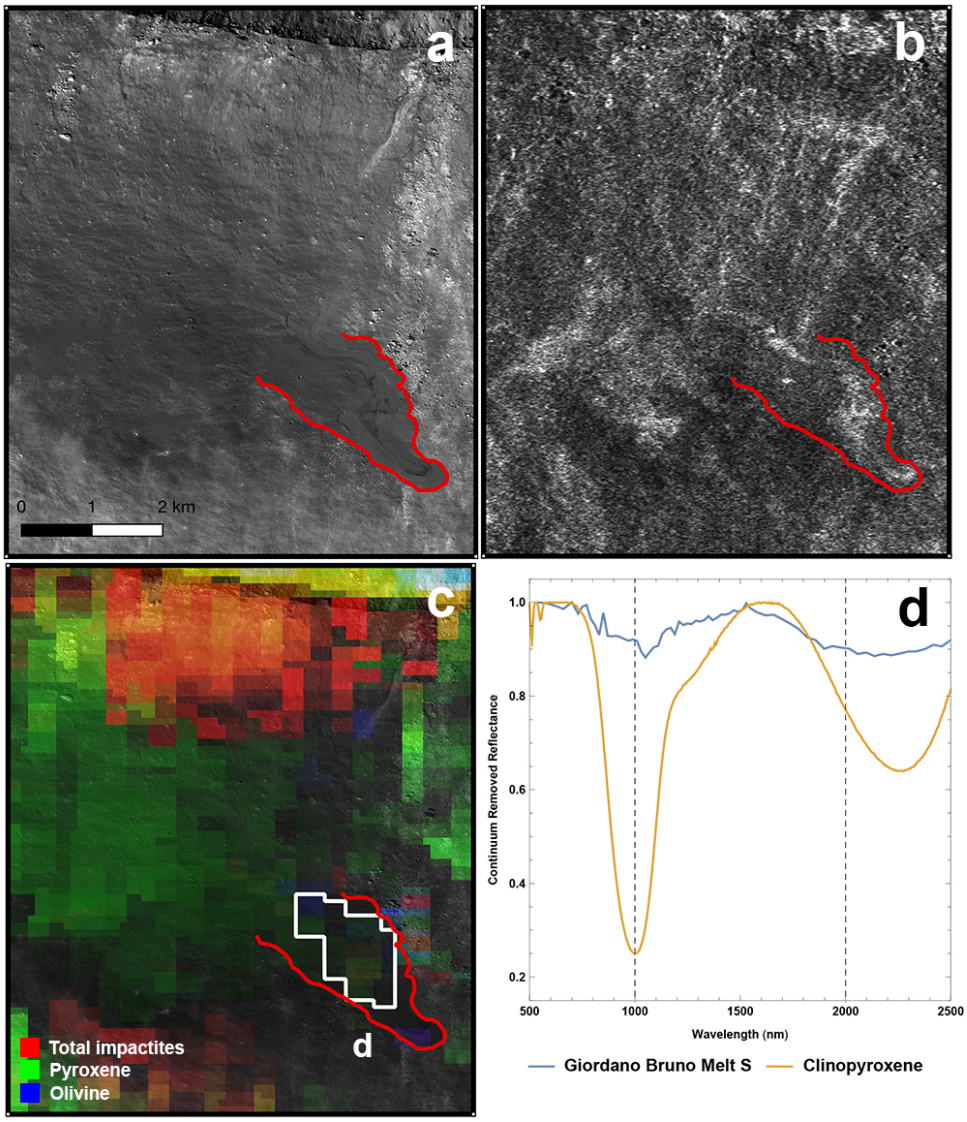

Figure 13: (a) LROC NAC image of a prominent melt flow emanating from the south rim of Giordano Bruno (M106209806RE.IMG). The lobate portion of the flow has been outlined in red. (b) Mini-RF total power image shows decimeter scale roughness variations in the melt deposit, in an otherwise rough ejecta blanket (LSZ_02525_1CD_XKU_37N103_V1.IMG). (c) Spectral unmixing results of this region suggest the flow is consistent with pyroxene (EM1), with some contribution from olivine (EM2). A white box indicates the region where the spectrum shown in (d) has been extracted. (d) Average continuum removed spectrum of a portion of the melt flow from Giordano Bruno (scaled by a factor of four for clarity), compared to a clinopyroxene spectrum given in Figure 4 (sample DL-CMP-057).

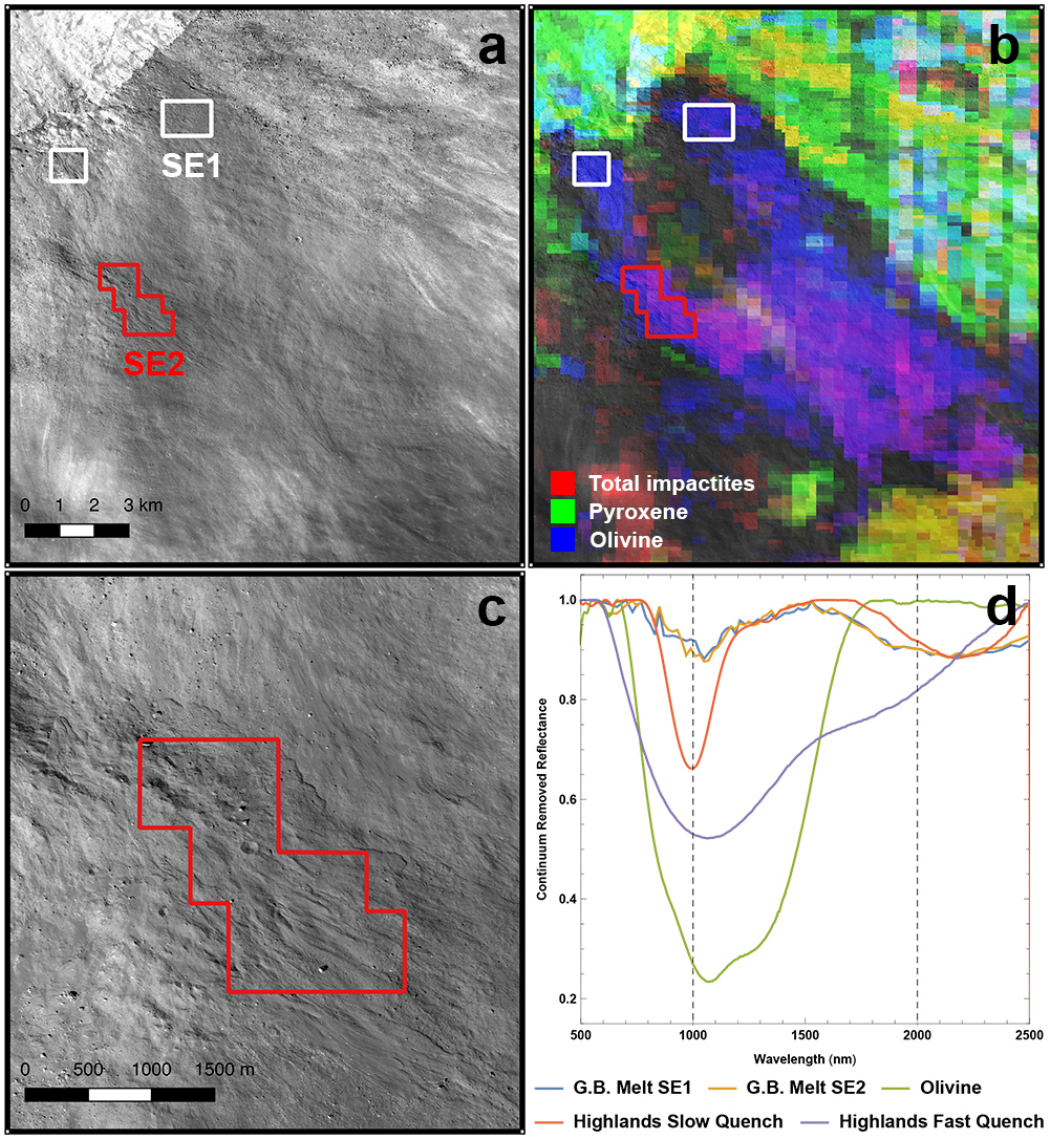

606
607 **Figure 14**: (a) LROC NAC image of melt flows and veneers emanating from the
608 southeast rim of Giordano Bruno (M106188285.IMG). (b) Spectral unmixing
609 results of this region suggest the flow is consistent with olivine (EM2), although
610 this is likely a misidentification. Boxes indicate the regions where the spectra
611 shown in (d) have been extracted. (c) Zoomed in image of region SE2,
612 highlighting the flow textures observed in this region. (d) Average continuum
613 removed spectrum of the Giordano Bruno melt deposits (scaled by a factor of four
614 for clarity), compared to an olivine spectrum (sample DD-MDD-001), the slow-
615 quenched synthetic highlands melt spectrum, and the fast-quenched synthetic
616 highlands glass spectrum shown in Figure 4.

3.4 The special case of Aristarchus

Aristarchus Crater is a 42 km diameter crater that formed on the southeastern margin of the Aristarchus Plateau. The Aristarchus Plateau and the ejecta of Aristarchus crater represent one of the most geologically diverse regions on the Moon, containing evidence for pyroclastic volcanic glasses, mare and plateau materials, and purported high-silica compositions [*Zisk et al*., 1977; *McEwen et al*., 1994; *Zhang and Jolliff*, 2008; *Glotch et al*., 2010; *Horgan et al*., 2014; *Zanetti*, 2015]. Geologic and geomorphologic mapping of the crater show a diverse array of impact melt morphologies around the crater (ponds, flows, and veneers) [*Zanetti*, 2015]. Melt deposits around Aristarchus do not show compositionally unique spectra, but rather appear to adopt compositions similar to the regions of the target from which they were derived [*Zanetti*, 2015].

The reasons for this are unclear, but potential explanations include (1) selective melting of the substrate, (2) recrystallization of the impact melt, and/or (3) the inclusion of lithic clasts during the transport and deposition of the impact melt. The shock metamorphic phenomenon referred to as selective mineral melting is where, for example, all the plagioclase in a rock would be converted into glass and any mafic minerals remain relatively intact; this is plausible as shock pressures need to be much higher to melt pyroxene and olivine when compared to plagioclase [see *French*, 1998]. However, since the range of shock

638 pressures needs to be quite limited (e.g., ~45-55 GPa), selective mineral melting
639 is quite rare amongst impact rocks. This likely rules out the chances of observing
640 a spectral signature of a melt deposit affected by selective mineral melting,
641 especially from orbit. Recrystallization of the melt is also an unlikely explanation.
642 Crystals formed from the cooling and re-crystallization of impact melts are
643 generally restricted to the interior of more voluminous and slowly cooled melt
644 sheets in basin forming impacts >300 km in diameter [e.g., *Vaughan et al.*, 2013].
645 In contrast, craters in this study are less than 100 km in diameter and observations
646 are mainly focused on the less voluminous terrace and exterior melt deposits. On
647 the other hand, the contamination of lithic clasts from the transport and deposition
648 of the impact melt outside of the walls of the transient cavity is likely to be a
649 major contributor to spectral signatures of melt deposits. Analysis of
650 hyperspectral data and high-resolution images of Martian complex craters show
651 that clast-bearing impact melt deposits typically adopt the spectral signature of the
652 materials they flowed over [e.g., *Hopkins et al.*, 2017].

653 Of particular interest at Aristarchus are ejecta deposits of similar
654 composition in the southwestern and eastern parts of the crater that have high
655 albedo and are highly correlated with high-silica Christiansen Feature (CF)
656 signatures in Diviner data [*Glotch et al*., 2010; *Zanetti*, 2015]. These areas have
657 been interpreted by previous researchers as impact melt glass [*Mustard et al*.,
658 2011], or spectrally neutral impact melt [*Horgan et al*., 2014]. However, although

659 some melt morphologies are present, detailed geomorphologic mapping showed
660 that these areas generally lack widespread flows, ponded melt, or evidence of
661 impact melt veneers. Rather, the correlation with high-silica and low-Fe ejecta
662 suggests that these regions are consistent with more evolved lithologies excavated
663 by the Aristarchus impact event [*Zanetti*, 2015].

664 When we compare the melt deposit map produced by *Zanetti* [2015] to our
665 spectral unmixing results (Figure 15), we find no correlation between the location
666 of the melt deposits and any specific spectral signature (Figure 16). In one
667 prominent melt deposit north of the crater (~16.5 km^2 in areal extent), the model
668 failed to identify any preferred endmember. As in the *Horgan et al.* [2014]
669 analysis, our unmixing model suggests the presence of impact melts and breccias
670 southwest of the crater. However, as we describe above, there is little
671 morphological evidence of widespread melt ponds or flows in this region. In
672 Figure 17, we highlight a region with no mapped melt deposits that has a spectral
673 signature consistent with impact melts/breccias. The band centers in this region
674 are found at 0.99 and 2.17 μm, compared to 0.99 and 2.19 μm for the slow-
675 quenched synthetic highlands melt. If melt is present, it must be a very thin layer,
676 or intimately mixed with the ejecta. However, it is also possible that the unusual
677 chemistry at the site of Aristarchus is producing spectrally bland signatures not
678 representative of compositions found elsewhere on the Moon, confusing spectral
679 models. Glass spectra tend to be low contrast and verging on spectrally bland

680 themselves, so any spectrally bland unit on the lunar surface can be matched to
681 these spectra. This result emphasizes the need to correlate spectral results to
682 mapping conducted using other data sets, which are capable of identifying
683 morphological evidence of impact melt deposits (such as high-resolution visible
684 imagery or radar data).

685 As in previous studies [e.g., *McEwen et al*., 1994; *Mustard et al.*, 2011;
686 *Horgan et al.*, 2014], we also identify olivine in a region southeast of the crater.
687 This region is associated with a comparatively low albedo portion of the ejecta
688 blanket (Figure 18). However, this region was investigated in high-resolution
689 NAC images and no melt veneers were identified based on their morphology
690 (although our spectral mixing model supports the presence of both olivine and
691 impactites in this region). As in the region southwest of the crater, if melt is
692 present, it must be thinner than the typical veneer or intimately mixed with the
693 ballistic component of the ejecta. Finally, the model identifies the presence of
694 quenched glass north of Aristarchus (Figure 15). This glass is associated with the
695 pyroclastic activity concentrated in this region [e.g., *Zisk et al*., 1977; *Gaddis et*
696 *al*., 1985; *Campbell et al*., 2008]. This identification gives us confidence that the
697 model can recognize quenched glass where present.

698 Note that we do not present radar data for Aristarchus here, because the
699 entire ejecta blanket is radar bright and it is therefore difficult to discern the radar
700 bright impact melt deposits from the radar bright blocky ejecta. See *Carter et al.*

[2017] for Arecibo and Mini-RF images of Aristarchus.

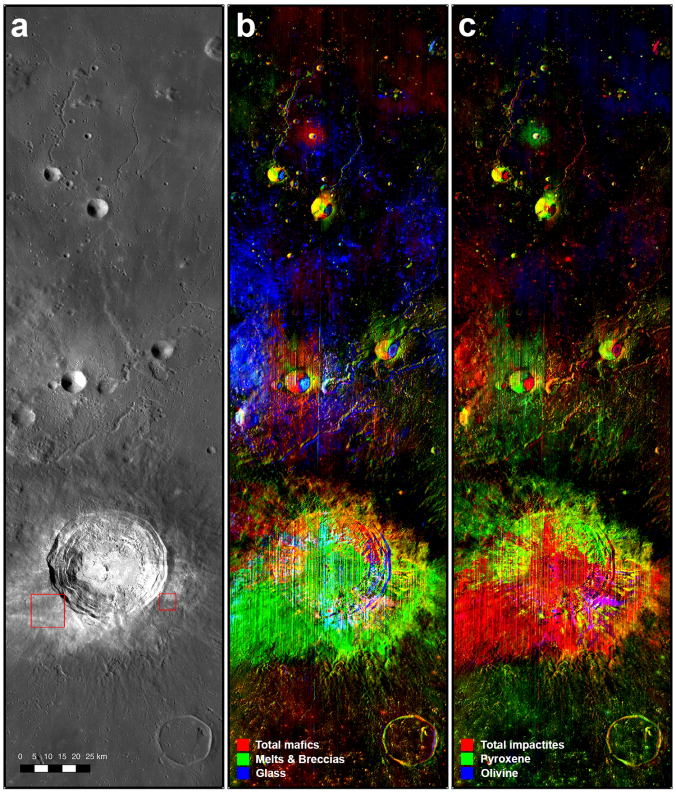

Figure 15: (a) LROC WAC mosaic of Aristarchus crater. The red boxes indicate the location of Figures 17 (left) and 18 (right). (b) Spectral unmixing results from the M^3 images M3G20090209T054031_V01_RFL.IMG and M3G20090209T072710_V01_RFL.IMG. Here, red represents the combined mafic endmembers (pyroxenes, EM1, and olivines, EM2), green represents impact melt and breccia endmembers (EM4), and blue represents quenched glass endmembers (EM3). (c) Spectral unmixing results, where red represents the combined impactite endmembers (quenched glass, EM3, and impact melts and breccias, EM4), green represents pyroxene-rich endmembers (EM1), and blue represents olivine-rich endmembers (EM2). All bands have been scaled linearly from 0.01 to their maximum value, to remove spuriously low values.

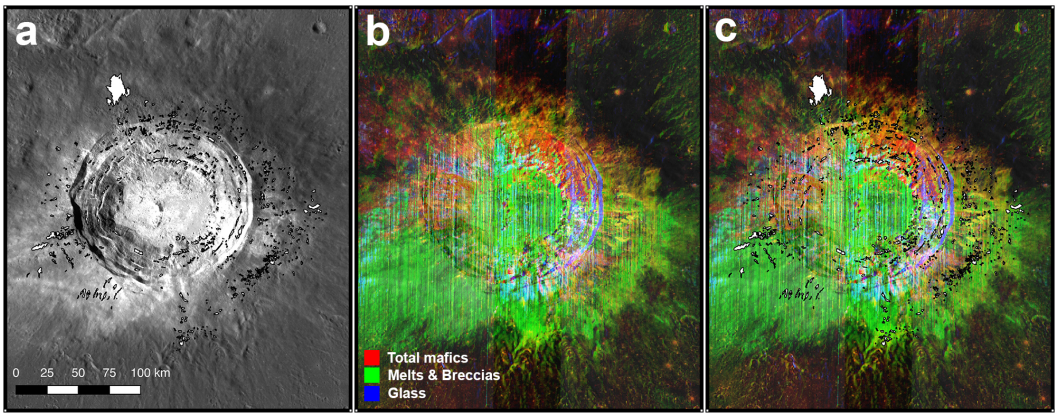

Figure 16: (a) LROC WAC mosaic of Aristarchus crater, showing the locations of melt deposits identified by *Zanetti* [2015]. The melt is shown in white with black outlines. (b) Spectral unmixing model results of the same region, without and (c) with the melt deposits labeled.

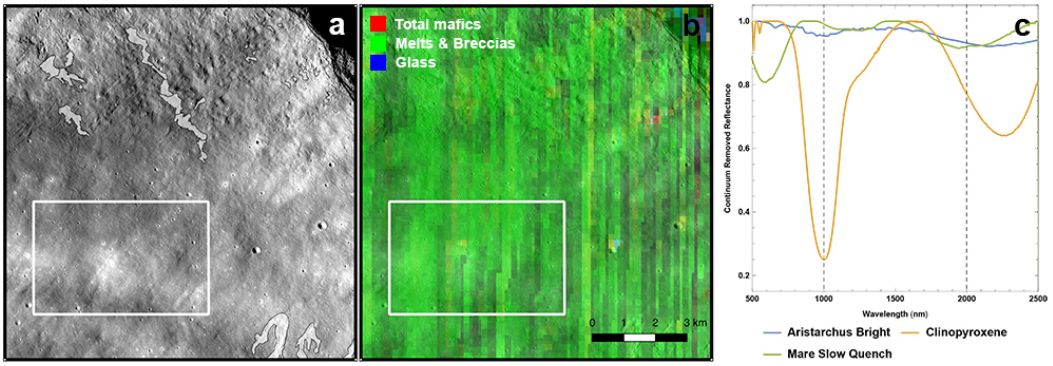

Figure 17: (a) LROC NAC image of the bright ejecta southwest of Aristarchus (M1096815140.IMG). Prominent melt deposits are identified in gray, and a box indicates the region where the spectrum shown in (c) has been extracted. (b) Spectral unmixing results of this region suggest the flow is consistent with impact melts and breccias (EM4). (c) Average continuum removed spectrum of the Aristarchus bright ejecta, compared to a clinopyroxene spectrum (sample DL-CMP-057) and the mare slow quench spectrum given in Figure 4.

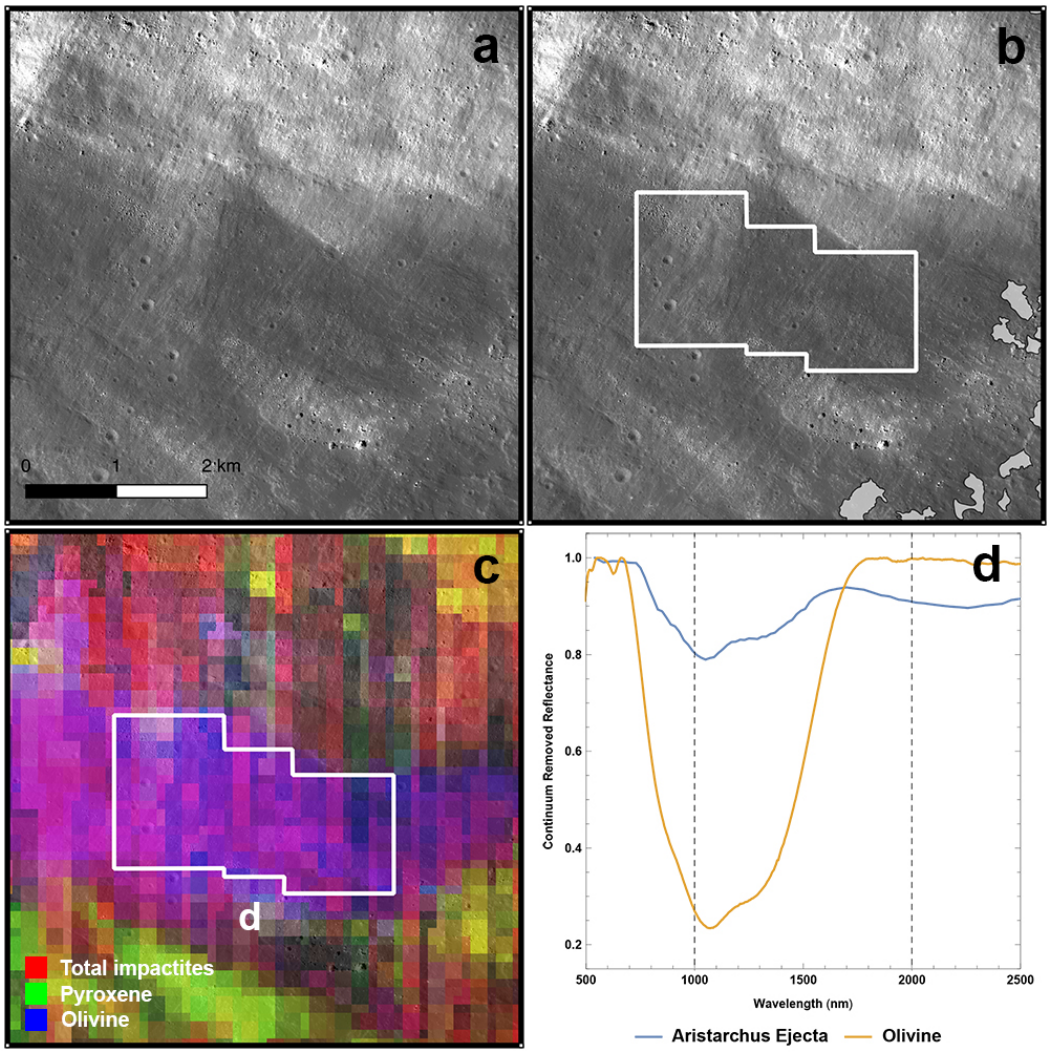

Figure 18: (a) LROC NAC image of an olivine-rich portion of the ejecta on the southeast rim of Aristarchus (M1191003838.IMG). (b) The same image from (a), with prominent melt deposits identified in gray. A box indicates the region where the spectrum shown in (d) has been extracted. (c) Spectral unmixing results of this region are consistent with the olivine endmember (EM2). (d) Average continuum removed spectrum of the Aristarchus ejecta, compared to an olivine spectrum from Figure 4 (sample DD-MDD-001).

742 *3.5 Glushko*

743

744 Glushko (formerly known as Olbers A) is a relatively young 43 km
745 diameter crater located near the highlands/mare boundary, likely Copernican in
746 age [*Neish et al*., 2013]. Extensive impact melts are observed to the north of the
747 crater rim [*Hawke and Head*, 1977], easily observed as radar bright deposits in S-
748 Band images of the Moon [*Campbell et al*., 2010; *Neish et al*., 2013]. The radar
749 data show a prominent lobate deposit flowing around local topography about 40
750 km north and west of the edge of the continuous ejecta blanket [*Campbell et al*.,
751 2010]. The Glushko melt flow has a circular polarization ratio near one at 70 cm
752 and in excess of one at 12.6 cm, indicating a blocky surface texture at the
753 decimeter to meter scale [*Campbell et al*., 2010].

754 This lobate deposit is also easily observed in our spectral unmixing model
755 results from the M^3 data in this region (Figure 19). This region is identified as
756 being spectrally consistent with impact melts and breccias, and is clearly distinct
757 in composition from the surrounding highlands terrain (Figure 20). We extracted
758 an average spectrum from a portion of this melt unit and find that it has spectral
759 characteristics that are most consistent with the melts plus breccias endmember
760 (EM4) (Figure 21). The band centers in this region are found at 1.00 and 2.24 μm,
761 compared to 1.00 and 2.26 μm for the clinopyroxene DL-CMP-057 and 0.99 and
762 2.19 μm for the slow-quenched synthetic highlands melt.

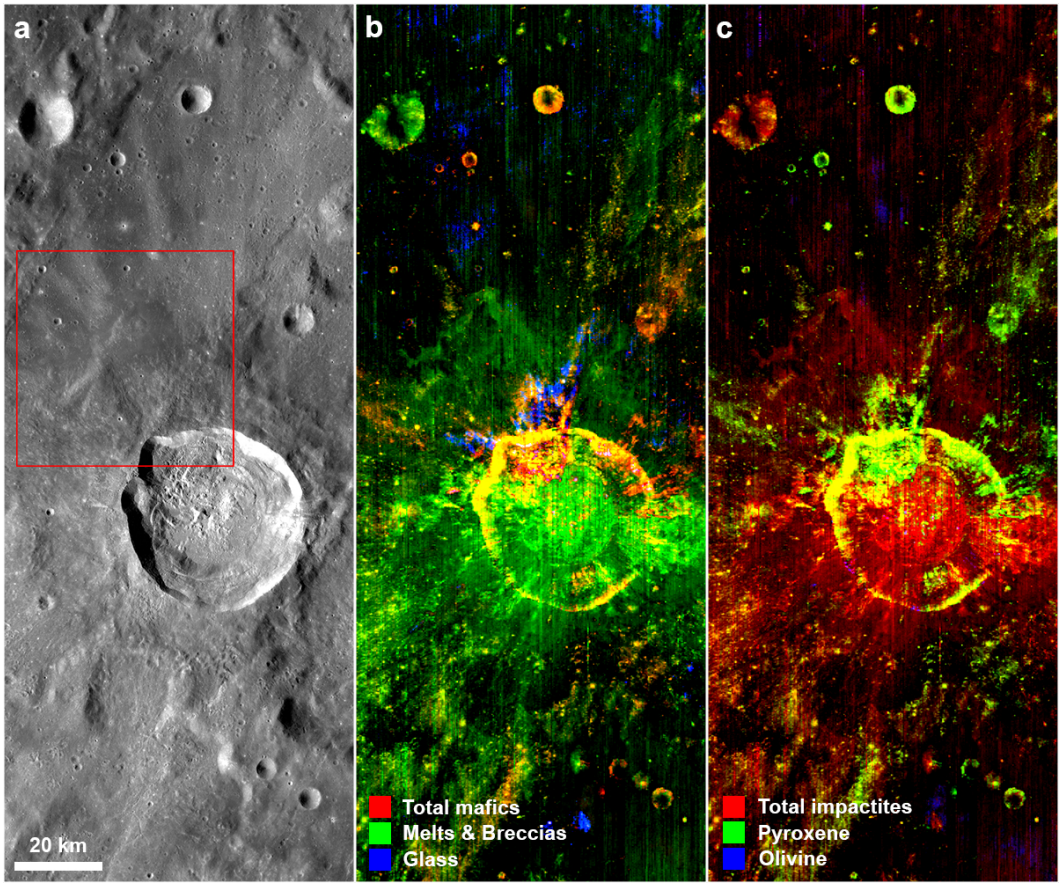

Figure 19: (a) LROC WAC mosaic of Glushko crater. The red box indicates the location of Figure 20. (b) Spectral unmixing results from the M^3 image M3G20090614T131003_V01_RFL.IMG. Here, red represents the combined mafic endmembers (pyroxenes, EM1, and olivines, EM2), green represents impact melt and breccia endmembers (EM4), and blue represents quenched glass endmembers (EM3). (Note: The blue streaks on the northern rim of Glushko are not observed in a higher-resolution M^3 image of the same region, and are likely the result of noise rather than a true glass signature; see Section 4.2) (c) Spectral unmixing results, where red represents the combined impactite endmembers (quenched glass, EM3, and impact melts and breccias, EM4), green represents pyroxene-rich endmembers (EM1), and blue represents olivine-rich endmembers (EM2). All bands have been scaled linearly from 0.01 to their maximum value, to remove spuriously low values.

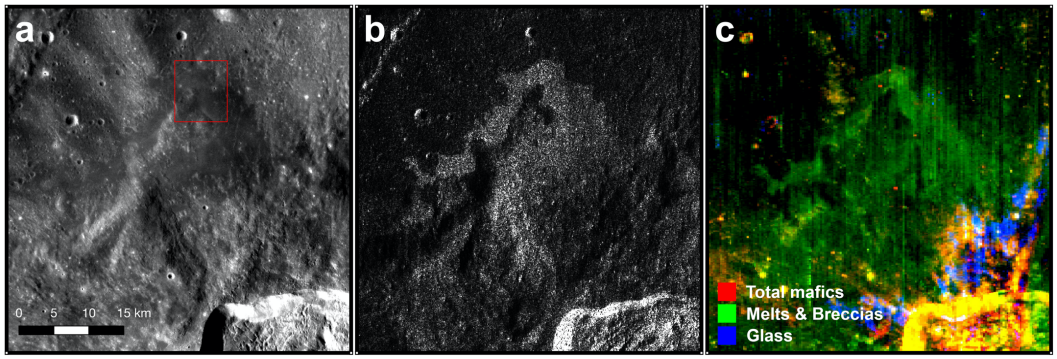

Figure 20: (a) LROC WAC mosaic of the melt flow north of Glushko crater. A red box indicates the location of Figure 21. (b) The melt flow is radar bright in an S-Band same sense radar backscatter image acquired from Arecibo (sband_12n270_scp.img), suggesting a blocky surface at the decimeter scale. (c) Spectral unmixing model results suggest the melt flow has a spectral signature consistent with the impact melts/breccia endmember (EM4).

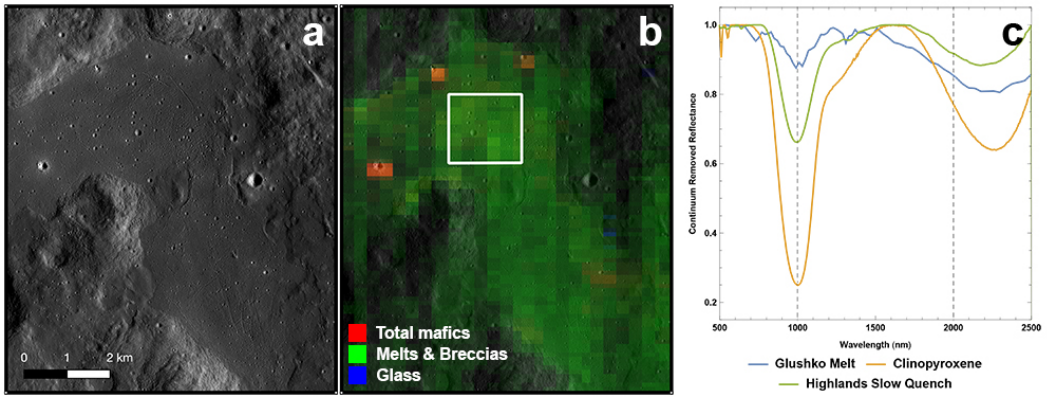

Figure 21: (a) LROC NAC image of a prominent melt flow emanating from the north rim of Glushko (M1108789729.IMG). (b) Spectral unmixing results of this region suggest the flow is consistent with the impact melts and melt breccias endmember (EM4). A white box indicates the region where the spectrum shown in (c) has been extracted. (c) Average continuum removed spectrum of a portion of the melt flow from Glushko (scaled by a factor of four for clarity), compared to a clinopyroxene spectrum (sample DL-CMP-057) and the highlands slow quench spectrum given in Figure 4.

797 *3.6 King*

798

799 King is a 76 km diameter complex crater located in the lunar highlands, of
800 Late Eratosthenian to Copernican age [*Ashley et al*., 2012]. King possesses a large
801 external deposit of impact melt to the north-northwest of the crater, ponded over
802 an area of ~300 km^2 [*Ashley et al.*, 2012]. Like most complex craters on the
803 Moon, the impact melt deposit is located just beyond the lowest portion of the
804 rim, likely pushed up and over the rim during the modification stage of impact
805 crater formation [*Neish et al*., 2014]. Known as the Al-Tusi melt pond, it is
806 characterized by flow features and viscoid forms, as well as hills and domes,
807 craters with anomalous morphologies, and negative relief features possibly
808 associated with near-surface caverns [*Hawke and Head*, 1977; *Heather and*
809 *Dunkin*, 2003; *Ashley et al*. 2012]. The melt pond has high radar backscatter and
810 circular polarization ratios, indicating that it is rough at the decimeter scale
811 (Figure 22).

812 When the spectral unmixing model is applied to a M^3 image of King
813 crater, the Al-Tusi melt pond does not appear to be consistent with any of the
814 endmembers used in our model (Figure 23). However, spectra from this region
815 suggest the presence of pyroxene, either in a pure form or mixed with low-
816 contrast glass or plagioclase (Figure 24). The band centers in this region are found
817 at 1.02 and 2.26 μm, compared to 1.00 and 2.26 μm for the clinopyroxene DL-

CMP-057. In addition, there is a sinuous feature connecting the crater to the melt pond. This feature has a spectral signature most consistent with pyroxene, with some contribution from melts plus breccias (Figure 24). The band centers here are comparable to those in the pond, at 1.01 and 2.24 μm. This feature may represent an outcrop of bedrock on the crater rim, exposing pyroxene, or possibly a melt flow contaminated with pyroxene-rich clasts. The addition of pyroxene-rich clasts would give the feature a different spectral signature than the surrounding melt deposits. The feature is not well-defined in the LROC NAC image, although evidence for melt is present in this region, including lower albedo and cooling cracks. The deposit appears to terminate in a lobate margin within the melt pond.

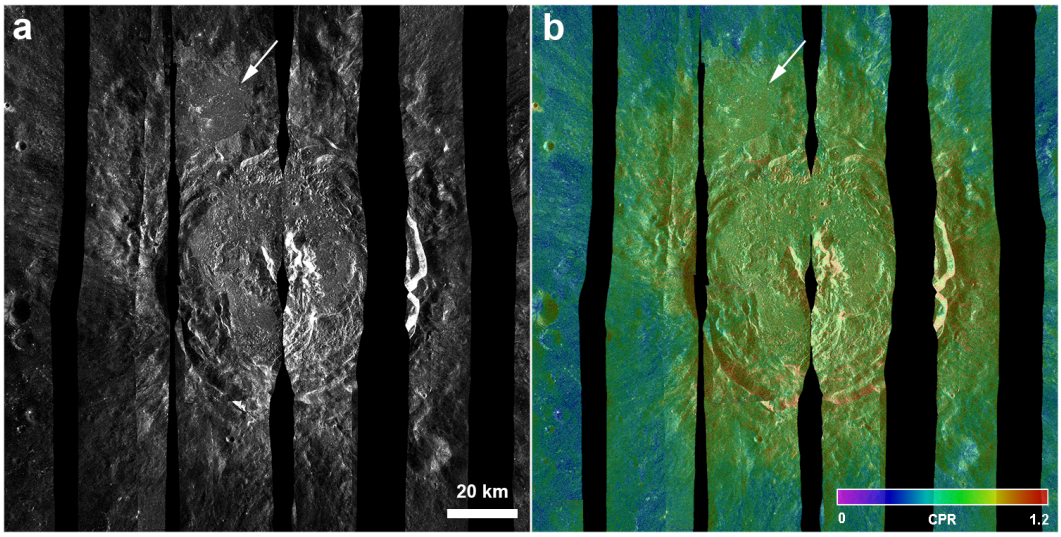

Figure 22: (a) Mini-RF same sense radar backscatter image of King crater. An arrow indicates the location of the Al-Tusi melt pond. (b) The high circular polarization ratio (CPR) of the melt pond indicates that it is rough at the decimeter scale.

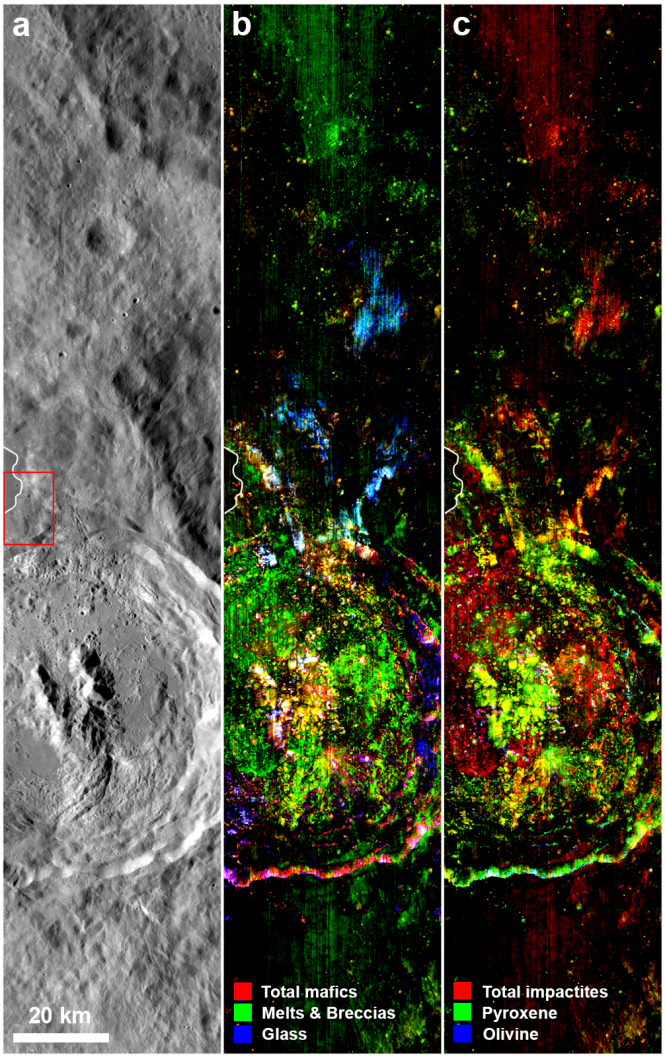

Figure 23: (a) LROC WAC mosaic of King crater. The red box indicates the location of Figure 24. The Al-Tusi melt pond is only partially covered in the scene and outlined in white. (b) Spectral unmixing results from the M^3 image M3G20081231T034148_V01_RFL.IMG. Here, red represents the combined mafic endmembers (pyroxenes, EM1, and olivines, EM2), green represents impact melt and breccia endmembers (EM4), and blue represents quenched glass endmembers (EM3). (c) Spectral unmixing results, where red represents the combined impactite endmembers (quenched glass, EM3, and impact melts and breccias, EM4), green represents pyroxene-rich endmembers (EM1), and blue represents olivine-rich endmembers (EM2). The red and blue bands in (b) and the green and blue bands in (c) have been scaled linearly from 0.01 to their maximum value, to remove spuriously low values. The green band in (b) and the red band in (c) have been scaled linearly from 0.05 to their maximum value.

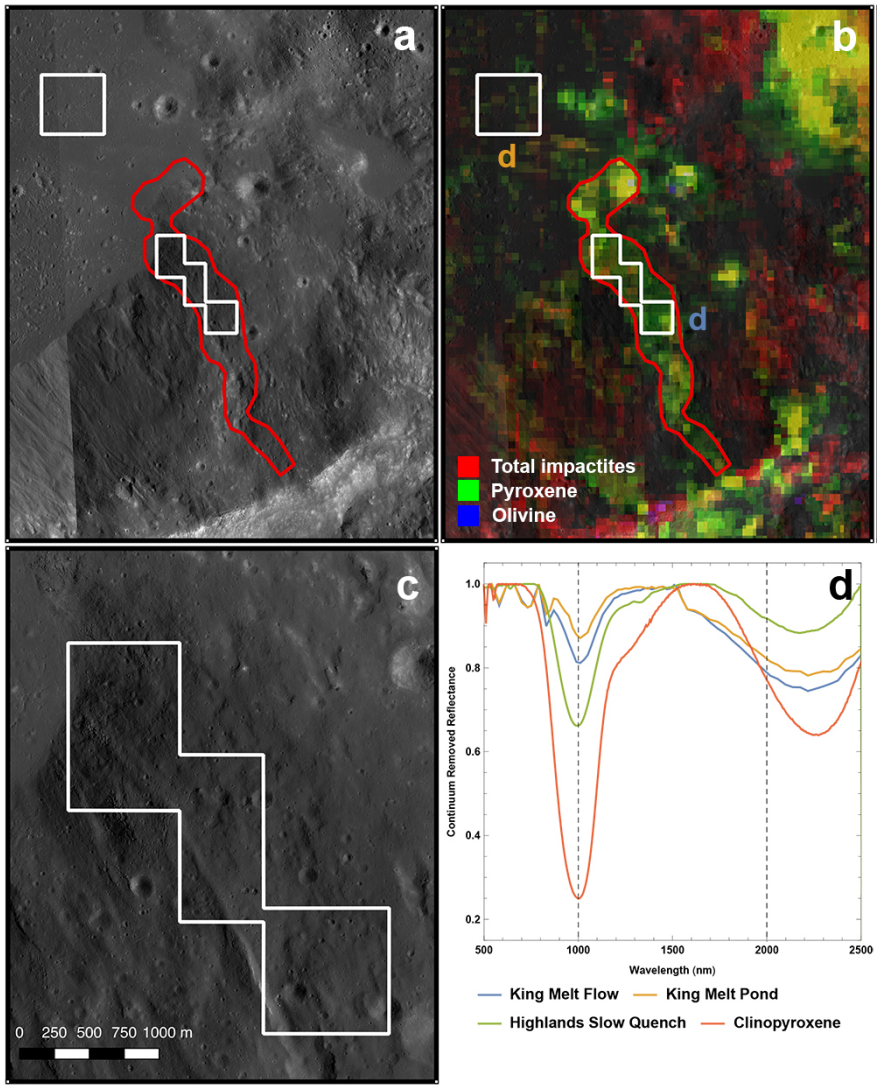

Figure 24: (a) LROC NAC mosaic of the north rim of King crater where it intersects with the melt pond (M103732241.IMG and M1138120053.IMG). The melt pond is located in the northwest portion of the image. A putative melt flow has been outlined in red. Boxes indicate the regions where the spectra shown in (d) have been extracted. (b) Spectral unmixing results of this region suggest the flow is consistent with the pyroxene endmember (EM1) with some contribution from the impact melt/breccia endmember (EM4). (c) Zoomed in image of the putative melt flow, highlighting the flow textures observed in this region. (d) Average continuum removed spectrum of the King melt pond and putative melt flow (scaled by a factor of four for clarity), compared to a clinopyroxene spectrum (sample DL-CMP-057) and the highlands slow quench spectrum given in Figure 4.

862 *3.7 Copernicus*

863

864 Copernicus is a 93 km diameter rayed crater in eastern Oceanus
865 Procellarum. Evidence for glass in the crater-fill deposits at Copernicus was first
866 argued for by *Smreker and Pieters* [1985]. Using ground-based near-infrared
867 spectra, they identified "anomalous" reflectance spectra on the floor of
868 Copernicus, characterized by a broad absorption line near one micron. They
869 interpreted these anomalous spectra as indicating the presence of pyroxene, Fe-
870 bearing glass, and Fe-bearing feldspar. More recent work by *Dhingra et al.* [2013]
871 using M^3 data also speculates on the presence of glass in the interior of
872 Copernicus crater, again noting the presence of a broad one-micron band in
873 certain regions.

874 When our spectral unmixing model is applied to the M^3 data in this crater,
875 several spectrally distinct regions are noted (Figure 25). First, the large
876 mineralogically distinct impact melt flow first described by *Dhingra et al.* [2013]
877 appears as a region consistent with pyroxene. This is in line with the
878 interpretations of *Dhingra et al.* [2013], who identified the flow as a Mg-rich
879 pyroxene. This region stands out in our spectral unmixing model because its
880 mineral composition differs from that of the surrounding rocks.

881 Second, two small impact craters just west of the flow have ejecta blankets
882 that are consistent with the quenched glass endmember (EM3). These craters were

883 also associated with broad one micron bands in *Dhingra et al.* [2013]. It is
884 possible that the craters generated glass-rich impact melt, which remains visible in
885 their ejecta blankets, or they are excavating glass rich materials from the
886 Copernicus melt sheet. Alternatively, the spectral interpretation of glass from the
887 unmixing model is incorrect. *Dhingra et al.* [2013] suggested this spectral feature
888 may also be consistent with clinopyroxene. Although the spectral features are not
889 as deep as those of a pure clinopyroxene spectrum, they do have similar band
890 centers (Figure 26). The band centers for this region are located at 1.00 and 2.16
891 μm, compared to 1.00 and 2.26 μm for the clinopyroxene DL-CMP-057 and 0.96
892 and 2.09 μm for the clinopyroxene DL-CMP-011.

893 Finally, a large melt flow emanating from the south rim of Copernicus is
894 spectrally consistent with the pyroxene endmember (Figure 27). As with the melt
895 flow at Donner M, this may not be a completely crystalline exposure of pyroxene,
896 but rather a mix of glass and pyroxene. The band centers for this region are
897 located at 0.96 and 2.18 μm, compared to 0.96 and 2.09 μm for the clinopyroxene
898 DL-CMP-011. The Mini-RF data in this region shows a high circular polarization
899 ratio, suggesting that the melt flow is rough at the decimeter scale (Figure 27).
900 Note that this melt flow is one of the only flows yet recognized with blocks
901 visible around its edges, likely increasing the CPR there. In addition, the steep
902 slopes associated with this flow will increase the local incidence angle of the
903 radar, which would increase its circular polarization ratio [see *Carter et al*., 2009].

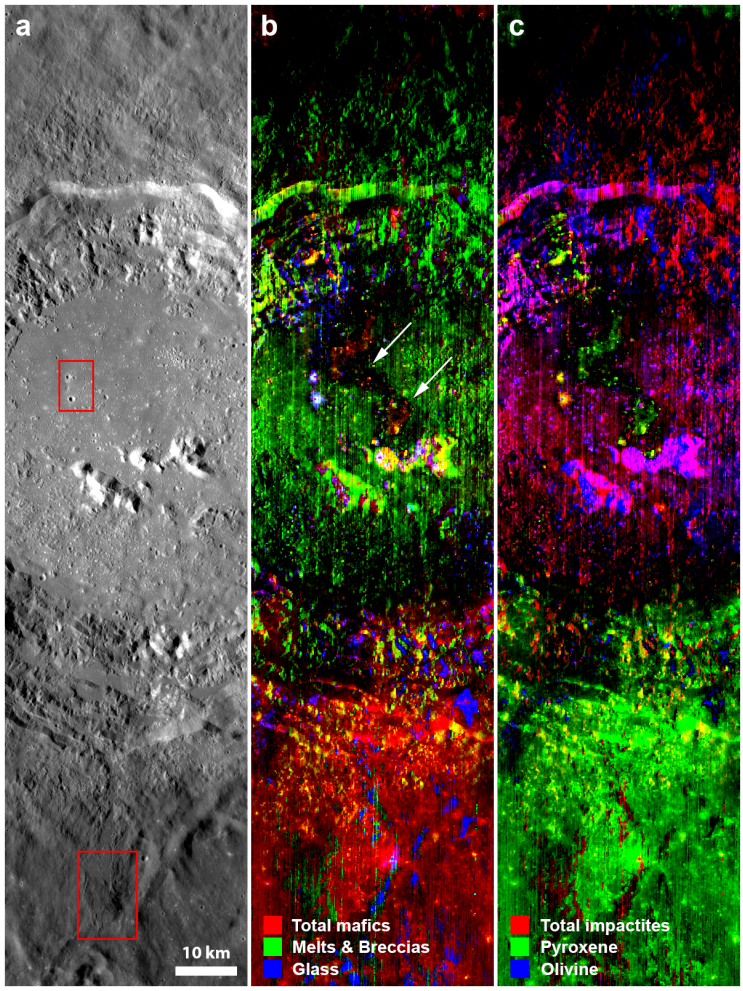

Figure 25: (a) LROC WAC mosaic of Copernicus crater. The red boxes indicate the location of Figures 26 (top) and 27 (bottom). (b) Spectral unmixing results from the M^3 image M3G20090207T044515_V01_RFL.IMG. Here, red represents the combined mafic endmembers (pyroxenes, EM1, and olivines, EM2), green represents impact melt and breccia endmembers (EM4), and blue represents quenched glass endmembers (EM3). White arrows indicate the mineralogically distinct melt flow first identified by *Dhingra et al.* [2013]. (c) Spectral unmixing results, where red represents the combined impactite endmembers (quenched glass, EM3, and impact melts and breccias, EM4), green represents pyroxene-rich endmembers (EM1), and blue represents olivine-rich endmembers (EM2). The red and blue bands in (b) and the green and blue bands in (c) have been scaled linearly from 0.01 to their maximum value, to remove spuriously low values. The green band in (b) and the red band in (c) have been scaled linearly from 0.1 to their maximum value.

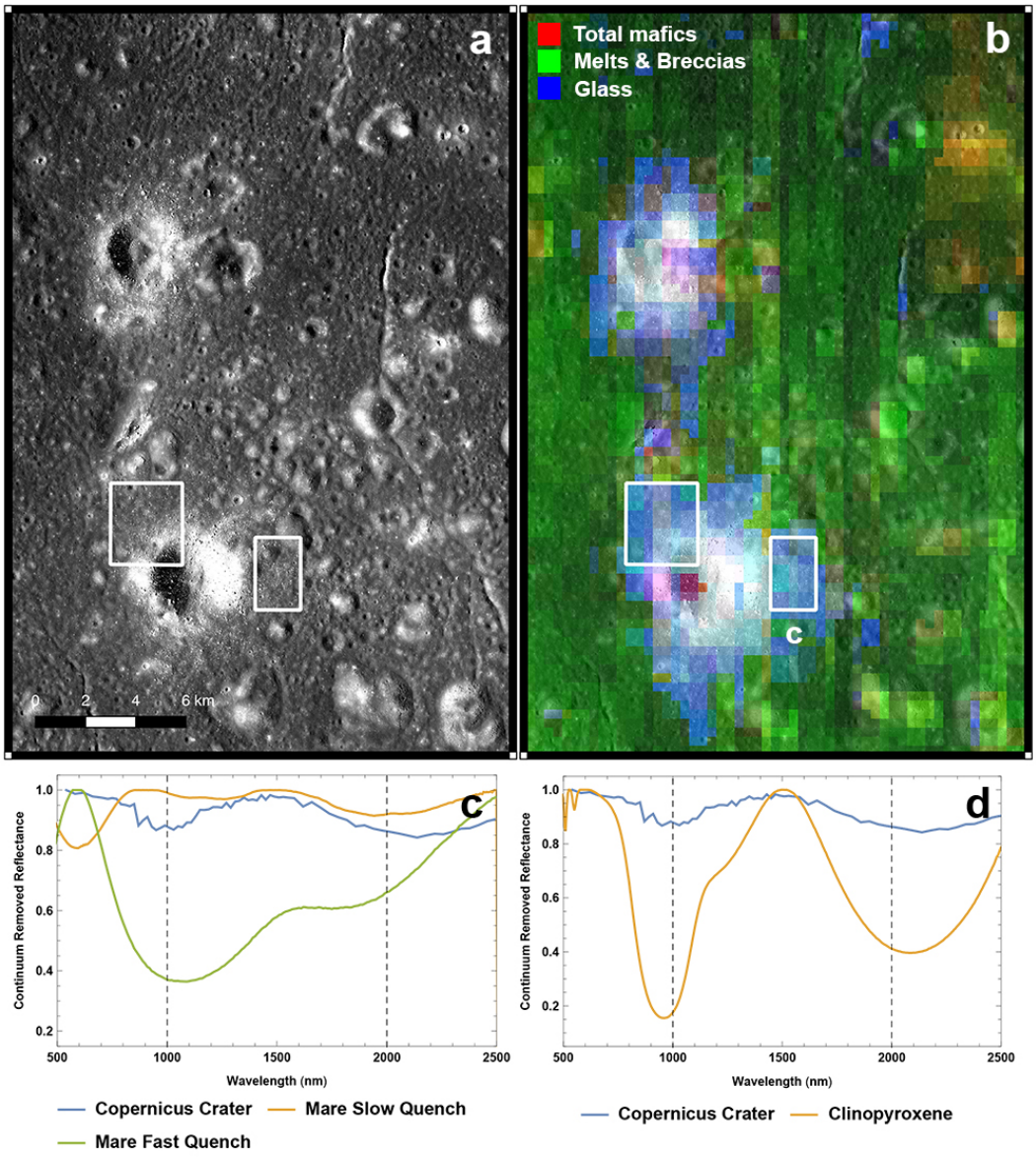

Figure 26: (a) LROC NAC image of a small crater located on the floor of Copernicus crater (M1175545925LE.IMG). (b) Spectral unmixing results of this region suggest the crater's ejecta is consistent with the quenched glass endmember (EM3). Two white boxes indicate the combined region where the spectrum shown in (c) and (d) was extracted. (c) Average continuum removed spectrum of a portion of the small Copernicus crater (scaled by a factor of two for clarity), compared to the slow-cooled mare melt and quenched mare glass given in Figure 4, and (d) a clinopyroxene spectrum from Figure 4 (sample DL-CMP-011).

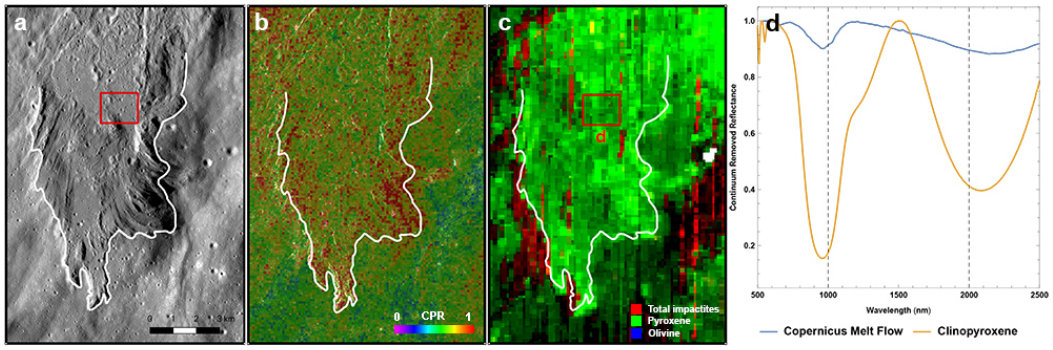

Figure 27: (a) LROC NAC image of a melt flow south of Copernicus crater (M1111947720.IMG). (b) This portion of the ejecta has a high circular polarization ratio (CPR) in an S-Band image acquired by Mini-RF (LSZ_02991_1CD_XKU_00S340_V1.IMG), suggesting a surface that is rough at the decimeter scale. (c) Spectral unmixing results of this region suggest the melt flow is consistent with the pyroxene endmember (EM1). A red box indicates where the spectrum shown in (d) was extracted. (d) Average continuum removed spectrum of the melt flow, compared to the a clinopyroxene spectrum from Figure 4 (sample DL-CMP-011).

4. Discussion

In this work, we examined the spectral characteristics of impact melt deposits around seven different lunar craters. We applied a spectral unmixing model to the data to determine the most likely spectral endmember groupings for the melt deposits around each crater. The four potential endmembers groups in our model included pure crystalline pyroxenes (EM1), pure crystalline olivines (EM2), fast-quenched synthetic lunar glasses (EM3), and impact melts and breccias (both synthetic and natural) (EM4). In all cases, the impact melt-bearing deposits were not consistent with the fast-quenched glass endmembers (EM3). Most were consistent with the pyroxene endmember (EM1), and some were consistent with the impact melts and breccia endmember (EM4). These latter endmembers are represented by both the Apollo samples and slow-quenched synthetic samples created for this work (see Table 1 and Figure 4). The partially glassy endmembers in EM4 are spectrally dominated by quench crystallites of pyroxene, but are distinct enough from pure crystalline pyroxene to be distinguishable in some cases (see Section 4.2 below). A summary of the results is presented in Table 3.

Table 3: Summary of the results of the spectral unmixing model.

Crater	Spectral Character of Melt Deposits in Model
Donner M	(EM1) Pyroxene (melt flow)
Tharp	(EM4) Melts + Breccias (melt pond) (EM1) Pyroxene (melt veneer)
Giordano Bruno	(EM1) Pyroxene (melt flow) (EM2) Olivine[a] (melt veneer)
Aristarchus	None (melts not consistent with any end member)
Glushko	(EM4) Melts + Breccias (melt flow)
King	None (Al-Tusi melt pond) (EM1) Pyroxene (possible melt flow)
Copernicus	(EM1) Pyroxene (interior and exterior melt flows)

[a]Olivine signature likely a false positive.

4.1 Interpretations of the results

We seek to use these results to infer the cause of the unusual roughness properties of lunar impact melt deposits. As previously mentioned, they appear exceptionally rough/blocky at the decimeter scale, but smooth at the meter scale. In *Neish et al.* [2017], we hypothesized that the melt flows may be similar to "transitional" pahoehoe lava flows on Earth. In these flows, initially smooth pahoehoe is mechanically fractured by later surges of lava to form "rubbly" or "slabby" forms of pahoehoe. We examined several terrestrial lava flows of this type in Hawai'i, Iceland, and Idaho and could find no analogues with similar roughness properties. The closest analogue was a rubbly lava flow in Iceland, but it only had moderate values of CPR when compared to the lunar melt deposits (~0.5 vs. 1).

977 Another hypothesis that we considered in *Neish et al.* [2017] was that the
978 radar was sensing the disrupted surface of the melt flow, broken apart by impact
979 gardening and covered with regolith. An S-Band radar such as Mini-RF can sense
980 decimeter-sized blocks buried up to ~1 m in lunar regolith. To test this
981 hypothesis, we compared the roughness properties of fresh impact melt deposits
982 to those of fresh lava flows on the Moon (specifically, Ina D). If they were formed
983 in the same way, impact gardening should affect them in a similar way. We found
984 that although the fresh lunar lava flows had similar roughness properties to the
985 fresh impact melt flow at the meter scale (similar RMS slope and Hurst
986 exponent), their radar properties were quite different. Ina D had low CPR values
987 at S-Band, similar to the surrounding regolith. This implies fresh lava flows and
988 fresh impact melt deposits are not emplaced in the same way on the Moon.
989 Indeed, there are several notable differences between the emplacement of
990 lava flows and impact melt deposits [*Osinski et al*., 2018]: (1) Impact melting
991 results in total melting, as opposed to partial melting of target rocks, (2) impact
992 melts may be superheated, while lava flows are erupted near the liquidus, and (3)
993 impact melts are clast-rich, while lava flows are not. With these differences in
994 mind, we investigate two new hypotheses to explain the surface texture of lunar
995 impact melt deposits in this work. In the first, we speculate that the entrainment of
996 clasts within the melt deposits might alter their surface texture. As discussed
997 above, melt deposits around Aristarchus crater and certain Martian craters adopt

998 the spectral signature of the surrounding materials [*Zanetti*, 2015; *Hopkins et al.*,
999 2017]. This may suggest that the spectra are dominated by the presence of clasts
1000 in the melt. However, we deem it unlikely that clasts would increase the
1001 decimeter-scale roughness of the melt surface, without also altering its meter-
1002 scale roughness. For example, at Mistastin crater on Earth, observed clasts range
1003 in size from centimeter to meter scale [*Grieve*, 1975; *Mader and Osinski*, 2018].
1004 So if clasts were the cause of the increased decimeter-scale roughness, we would
1005 expect a similar increase in meter-scale roughness.

1006 In the second hypothesis, we suggest that the different cooling history
1007 experienced by lunar impact melt produces a glassier surface layer than that found
1008 in lunar lava flows. Although we find no spectral evidence of fast-quenched
1009 glasses in the melt deposits (similar to those found in pyroclastic deposits), we do
1010 find spectra that are consistent with the slow-cooled synthetic melts and/or
1011 returned samples of impact melt breccias from the Moon. In this scenario, a
1012 surficial layer may form on the melt deposits that contains both glass and fine-
1013 grained crystals of minerals including pyroxene, olivine, and plagioclase. As we
1014 discussed previously, a sample with more than 60% glass is necessary for the
1015 presence of glass to be obvious in a mixed spectrum with pyroxene [*Tompkins*
1016 *and Pieters*, 2010]. Conversely, pyroxene is spectrally dominant at just 2 vol. %
1017 abundance in pyroxene-plagioclase mixtures [*Cheek and Pieters*, 2014]. This
1018 glassy surficial layer would lie on top of a more crystalline subsurface deposit,

1019 which experienced a slower cooling rate. If this surface layer is later disrupted
1020 through impact gardening or explosive degassing of vesicles, it may form a
1021 blocky layer over a melt flow that remains smooth at the meter scale (Figure 28).

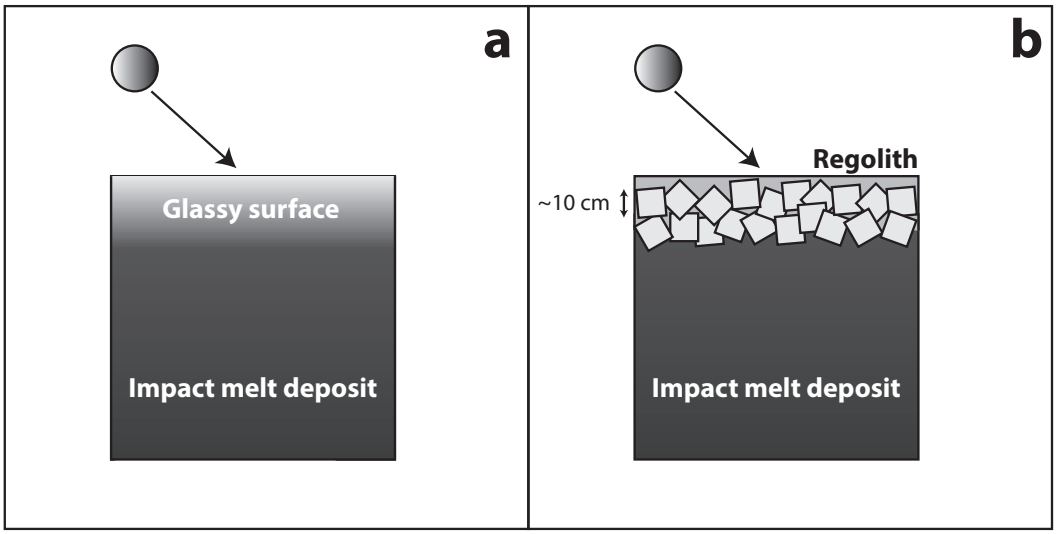

1022
1023 **Figure 28**: A hypothesis for the formation of impact melt deposits on the Moon.
1024 (a) A melt flow that is smooth at the meter scale is emplaced on the lunar surface.
1025 Faster cooling rates near the surface formed a glass-rich layer, overlying a more
1026 crystalline deposit. (b) Over time, impact gardening disrupts the glassy layer,
1027 shattering it into small blocks, which are eventually covered by regolith. The end
1028 result is a surface layer that is smooth at the meter scale, but rough at the
1029 decimeter scale.
1030

1031 This scenario is consistent with the observed morphology and topography
1032 of melt flows at the meter scale, while maintaining the high decimeter scale
1033 roughness observed by radar [*Neish et al*., 2017]. A glassy layer is more brittle
1034 than crystalline lunar rocks, and thus, is more likely to be disrupted to form flat
1035 cleavage surfaces that can act as corner reflectors (see Figure 2). Scattering from
1036 natural corner reflectors increases the circular polarization ratio of the signal

1037 [*Campbell et al.*, 2012] to the values observed by Arecibo and Mini-RF of the
1038 melt deposits [*Campbell et al*., 2010; *Neish et al.*, 2017].

1039 There is evidence in the Apollo collection that supports this hypothesis,
1040 including rare examples of glassy impact melt rocks [*Osinski et al.*, 2018]. For
1041 example, sample 64455 from the Apollo 16 collection is a 5 cm long egg-shaped
1042 object almost completely covered with black glass up to a cm in thickness, with
1043 small vesicles concentrated along the basalt/glass contact [*Ryder and Norman*,
1044 1980; Figure 29]. Most of these glassy impact melt rocks are not completely
1045 composed of glass, but also show evidence of micron-sized microlites, commonly
1046 clinopyroxene and plagioclase. This is consistent with our spectral analyses of
1047 lunar impact melt deposits. Still, one may wonder why such samples are so rare,
1048 given the large amount of impact melt present on the lunar surface [e.g., *Campbell*
1049 *et al*., 2018]. It is possible that these samples are not more common because they
1050 are so easily broken down by impact gardening. For example, the impact melt
1051 flow at Korolev Z (Figure 1) has a lower rock abundance in the Diviner data than
1052 other portions of its ejecta blanket [*Neish et al.*, 2017]. *Bandfield et al.* [2011]
1053 suggested that the low rock abundance observed over many lunar impact melt
1054 deposits implies that these deposits have mechanical properties that result in a
1055 more rapid development of regolith cover. Any glass present may be quickly
1056 processed into a fine particulate layer overlying a buried layer of decimeter sized
1057 blocks.

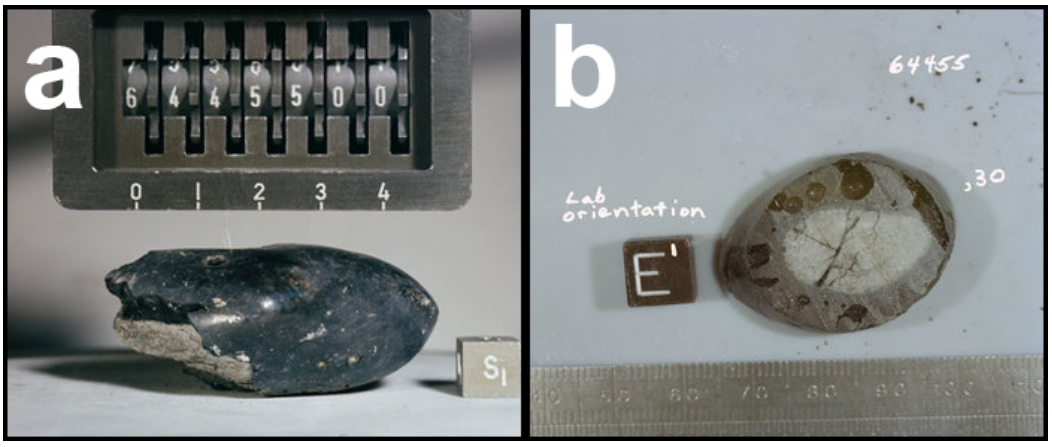

Figure 29: (a) Photograph of Apollo 16 sample 64455,0, with a 1 cm scale cube at lower right (photo number S72-43254B). This sample is almost entirely covered in black glass. (b) Photograph of Apollo 16 sample 64455,30, with ruler for scale. This photograph shows the interior structure of the sample, demonstrating a glass thickness of up to ~1 cm (photo number S91-36325). Source: NASA/JSC.

4.2 Limitations to the technique

There are some limitations to the spectral unmixing model used in this work that bear discussion. For example, if a spectral feature is ubiquitous and part of the "background" of the entire scene, then the model may not pick it out as being distinct because it uses spectra from the scene itself as an endmember. Thus, any impact melt deposits that have spectral properties similar to the background may not show a preferred endmember. Some of the melts identified at Aristarchus or the Al-Tusi melt pond at King may fall into this category. In

addition, any regions that are spectrally bland, with broad but weak one and two micron bands, are difficult to confidently assign to an endmember. Thus in some cases, there are likely false positive results (such as the "olivine" detection at Giordano Bruno) where the spectral model attempted to assign an endmember to a region that does not show distinct spectral features. Given the lack of spectral features in these regions, it is difficult to confidently identify what species may be present, but glass, plagioclase, or spectral mixtures are a few possibilities.

We also see differences in the model outputs when we include additional endmembers. For example, we get different results when we fit the data to three endmembers (EM1, EM2, and EM3) instead of four (Figure 30). We can see that with only three end members, the region southwest of Aristarchus is not fit by any of the endmembers, but when we include the fourth endmember, the model finds a fit to the melts plus breccias end member (EM4). The fact that the new endmember is fit is a unique indication that something distinct is present, because an F-test is used in the inverse model. If the new endmember didn't improve the model fit with statistical significance, it would not be modeled. Thus, it is important to utilize all reasonable endmembers when utilizing this model in order to best constrain the composition of the lunar surface.

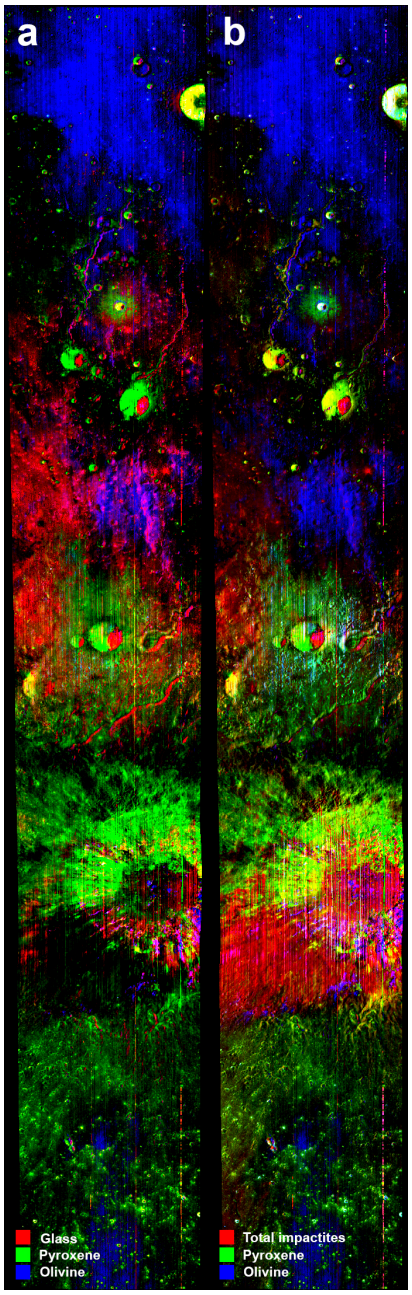

Figure 30: A comparison of the model results from a fit of M3G20090209T072710_V01_RFL.IMG with (a) three end-members (glass, pyroxene, and olivine) and (b) four end-members (glass, pyroxene, olivine, and melts plus breccias). In (b), glass (EM3) and melts plus breccias (EM4) have been combined into "total impactites".

1101 The resolution of the images may also play a role in the results of our
1102 model. Between optical period 2A and 2B, the orbit of the Chandrayaan-1
1103 spacecraft was increased, which reduced the resolution of the images by a factor
1104 of two. Roughly half of our images are from the lower resolution optical periods.
1105 To determine if this has affected our results, we compared the model outputs from
1106 two images acquired from the same region of Glushko crater (Figure 31). The
1107 model fits from the two different resolutions are similar, although there are a few
1108 regions where they differ (e.g., the ejecta north of the crater). We judge that the
1109 blue streaks on the northern rim of Glushko in the lower resolution image are
1110 likely the result of noise rather than a true glass signature, since they are not
1111 observed in the higher-resolution M^3 image. However, the melt flow of interest is
1112 fit to the melts and breccias end member (EM4) in both images, giving us
1113 confidence in the results in the region of interest.
1114
1115

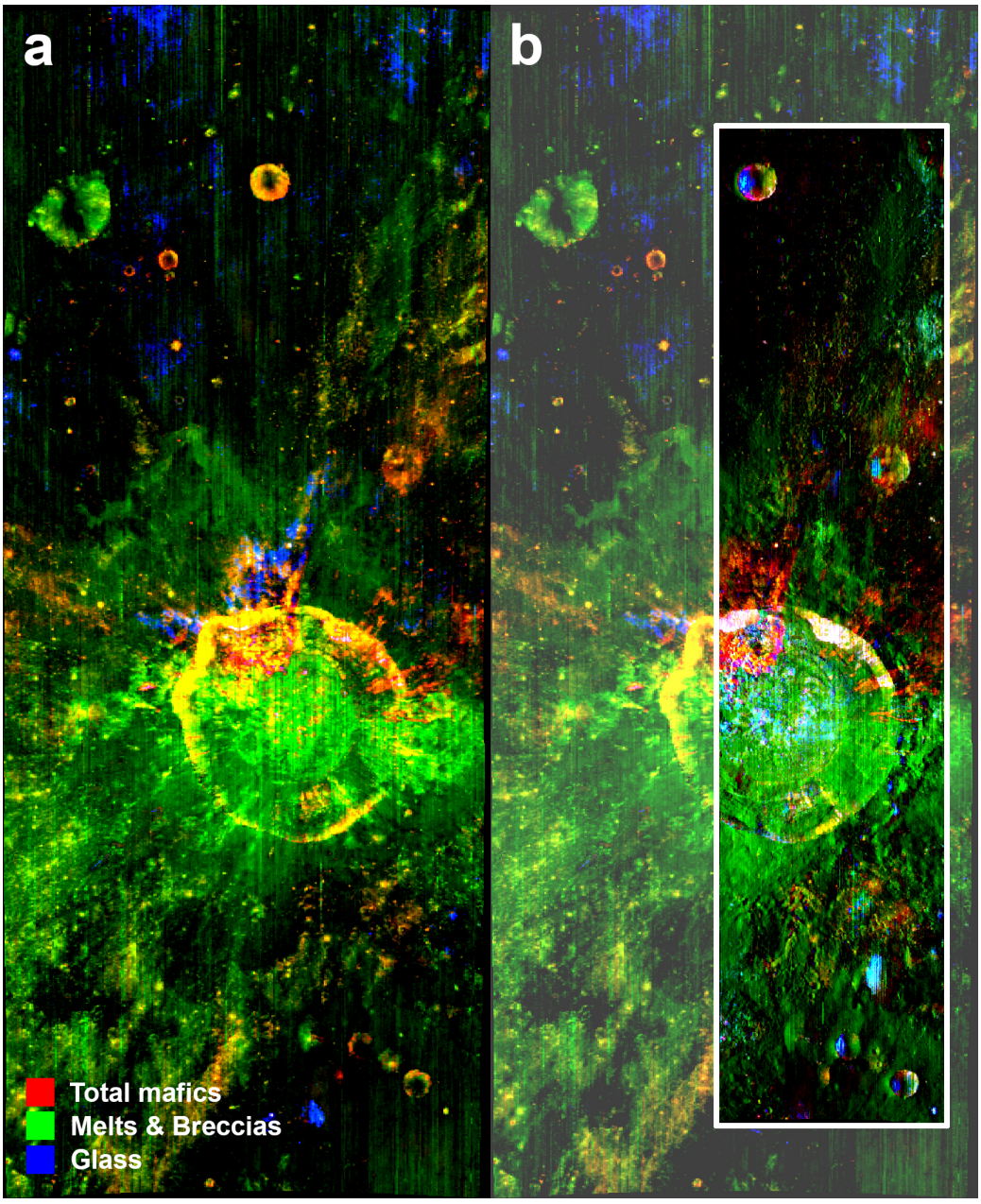

Figure 31: M^3 images of Glushko crater taken during (a) optical period 2C (M3G20090614T131003_V01_RFL.IMG; 280 m/pixel) and (b) optical period 2A (M3G20090614T131003_V01_RFL.IMG; 140 m/pixel). In (b), the higher resolution image is overlain on the lower resolution image of the same region. Both images are scaled linearly from 0.01 to their maximum value, to remove spuriously low values.

Finally, we note that our sample size was limited to only seven craters, and could be expanded to include more of the impact-melt bearing craters identified by *Neish et al.* [2014]. (However, some craters closer to the poles have lighting issues that would make this analysis difficult.) It would be particularly interesting to compare the results of highlands melt deposits versus those in the mare. For example, a recent study by *Morrison et al.* [2019] studied the crystallization of melted highlands and mare simulants. They found that highlands simulants have a higher melting point than mare simulants (~1325°C for mare-like basaltic JSC-1a vs. >1450°C for highlands-like norite and anorthite). They also demonstrated that anorthite and norite samples crystallize over a very narrow temperature interval after crossing the liquidus, whereas basaltic samples experience a more moderate amount of crystallization before experiencing a rapid increase after ~125°C of undercooling. Thus, if melts are quenched at a given temperature during cooling, a highlands melt deposit may contain more crystalline material than a mare melt deposit.

5. Conclusions

We examined the spectral characteristics of seven impact melt bearing craters on the Moon. We utilized a spectral unmixing model to look for evidence of one of four endmember groups in the melt deposits: pyroxenes, olivines, fast-

quenched lunar glass simulants, and impact melts and breccias (both synthetic and natural). We found that the majority of the melt deposits were spectrally dominated by pyroxene, consistent with the pyroxene and/or impact melts plus breccia endmembers. This suggests that the melt deposits are either crystalline deposits of pyroxene-rich rocks, a mixture of impact melt and pyroxene-rich lithic clasts, or a glassy material that contains pyroxene minerals in the form of quench crystallites. The latter interpretation is most consistent with the Mini-RF observations, which show extremely high decimeter-scale roughness. This roughness could be the result of a glassy surficial layer shattering during impact gardening to produce decimeter scale blocks over a deposit that remains smooth at the meter scale. This suggests that impact melt deposits on the Moon likely experience different cooling conditions compared to lunar lava flows, given their unique melting and emplacement conditions.

Acknowledgments

We thank the LRO and Chandrayaan-1 projects for their efforts in returning the data presented here. We also thank R. Wysocki and J. Karson of the Syracuse Lava Project for hosting us at their facility in October 2017, a visit which ultimately inspired this work. Finally, we thank J. Molaro for helpful conversations about rock failure, and B. Horgan, M. McBride, S. Besse, and an anonymous reviewer for suggestions that significantly improved the manuscript. C.N. and M.Z. were supported by an NSERC Discovery grant.

References

Altindag, R. (2010). Reply to the discussion by Yagiz on "Assessment of some brittleness indexes in rock-drilling efficiency". *Rock Mechanics and Rock Engineering*, *43*, 375-376.

Ashley, J. W., Robinson, M. S., Hawke, B. R., van der Bogert, C. H., Hiesinger, H., Sato, H., Speyerer, E. J., Enns, A. C., Wagner, R. V., Young, K. E., Burns, K. N. (2012). Geology of the King crater region: New insights into impact melt dynamics on the Moon. *Journal of Geophysical Research*, *117*, E00H29, doi:10.1029/2011JE003990.

Ashworth, D. G. (1978). Lunar and planetary impact erosion. In: J.A.M. McDonnell (Ed.), Cosmic Dust. John Wiley, Hoboken, NJ, pp. 427–526

Bandfield, J. L., Ghent, R. R., Vasavada, A. R., Paige, D. A., Lawrence, S. J., Robinson, M. S. (2011). Lunar surface rock abundance and regolith fines temperatures derived from LRO Diviner Radiometer data. *Journal of Geophysical Research, 116*, E00H02, doi:10.1029/2011JE003866.

1188 Besse, S., Sunshine, J.M., Staid, M.I., Petro, N.E., Boardman, J.W., Green, R.O.,
1189 Head, J.W., Isaacson, P.J., Mustard, J.F. and Pieters, C.M. (2011). Compositional
1190 variability of the Marius Hills volcanic complex from the Moon Mineralogy
1191 Mapper (M3). *Journal of Geophysical Research: Planets*, *116*(E6).
1192
1193 Besse, S., Sunshine, J., Staid, M., Boardman, J., Pieters, C., Guasqui, P., Malaret,
1194 E., McLaughlin, S., Yokota, Y., Li, J.Y. (2013). A visible and near-infrared
1195 photometric correction for Moon Mineralogy Mapper (M3). *Icarus*, *222*, 229-242.
1196
1197 Besse, S., Sunshine, J. M., Gaddis, L. R. (2014). Volcanic glass signatures in
1198 spectroscopic survey of newly proposed lunar pyroclastic deposits. *Journal of*
1199 *Geophysical Research: Planets*, *119*, 355-372.
1200
1201 Bhiravarasu, S. Bhattacharya, S. Chauhan, P. (2017). Giordano Bruno crater on
1202 the Moon: Detection and Mapping of Hydration Features of Endogenic and/or
1203 Exogenic Nature. AAS Division for Planetary Sciences Meeting Abstracts, 49,
1204 404.05.
1205
1206 Bray, V. J., Tornabene, L. L., Keszthelyi, L. P., McEwen, A. S., Hawke, B. R.,
1207 Giguere, T. A., Kattenhorn, S. A., Garry, W. B., Rizk, B., Caudill, C. M., Gaddis,
1208 L. R., and van der Bogert, C. H. (2010). New insight into lunar impact melt

1209 mobility from the LRO camera. *Geophysical Research Letters*, *37*, L21202,
1210 doi:10.1029/2010GL044666.
1211
1212 Campbell, B. A., Carter, L. M., Hawke, B. R., Campbell, D. B., Ghent, R. R.
1213 (2008). Volcanic and impact deposits of the Moon's Aristarchus Plateau: A new
1214 view from Earth-based radar images. *Geology, 36,* 135-138,
1215 doi:10.1130/G24310A.
1216
1217 Campbell, B. A., Hawke, B. R., Carter, L. M., Ghent, R. R., Campbell, D. B.
1218 (2009). Rugged lava flows on the Moon revealed by Earth-based radar.
1219 *Geophysical Research Letters*, *36*(22).
1220
1221 Campbell, B. A., Carter, L. M., Campbell, D. B., Nolan, M., Chandler, J., Ghent,
1222 R. R., Hawke, B. R., Anderson, R. F., Wells, K. (2010). Earth-based 12.6-cm
1223 wavelength radar mapping of the Moon: New views of impact melt distribution
1224 and mare physical properties. *Icarus*, *208*, 565–573,
1225 doi:10.1016/j.icarus.2010.03.011.
1226

1227 Campbell, B. A. (2012). High circular polarization ratios in radar scattering from
1228 geologic targets. *Journal of Geophysical Research*, *117*, E06008,
1229 doi:10.1029/2012JE004061
1230
1231 Campbell, B. A., Weitz, C. M., Whitten, J. L., Morgan, G. A. (2018). Evidence
1232 for impact melt sheets in lunar highland smooth plains and implications for polar
1233 landing sites. *Icarus*, *314*, 294-298.
1234
1235 Cannon, K. M., Mustard, J. F. (2015). Preserved glass-rich impactites on Mars.
1236 *Geology*, *43*, 635–638, doi:10.1130/G36953.1.
1237
1238 Cannon, K. M., Mustard, J. F., Parman, S. W., Sklute, E. C., Dyar, M. D., Cooper,
1239 R. F. (2017). Spectral properties of Martian and other planetary glasses and their
1240 detection in remotely sensed data. *Journal of Geophysical Research-Planets*, *122*,
1241 249–268, doi:10.1002/2016JE005219.
1242
1243 Carter, L. M., Campbell, B. A., Hawke, B. R., Campbell, D. B., Nolan, M. C.
1244 (2009). Radar remote sensing of pyroclastic deposits in the southern Mare
1245 Serenitatis and Mare Vaporum regions of the Moon. *Journal of Geophysical*
1246 *Research: Planets*, *114*(E11).
1247

Carter, L. M., Neish, C. D., Bussey, D. B. J., Spudis, P. D., Patterson, G. W., Cahill, J. T., Raney, R. K. (2012). Initial observations of lunar impact melts and ejecta flows with the Mini-RF radar. *Journal of Geophysical Research*, *117*, E00H09, doi:10.1029/2011JE003911.

Carter, L. M., Campbell, B. A., Neish, C. D., Nolan, M. C., Patterson, G. W., Jensen, J. R., Bussey, D. B. J. (2017). A Comparison of Radar Polarimetry Data of the Moon From the LRO Mini-RF Instrument and Earth-Based Systems. *IEEE Transactions on Geoscience and Remote Sensing*, *55*, 1915–1927, doi:10.1109/TGRS.2016.2631144.

Cheek, L. C., Pieters, C. M. (2014). Reflectance spectroscopy of plagioclase-dominated mineral mixtures: Implications for characterizing lunar anorthosites remotely. *American Mineralogist*, *99*, 1871–1892, doi:10.2138/am-2014-4785.

Clark, R. N., Pieters, C. M., Green, R. O., Boardman, J. W., Petro, N. E. (2011). Thermal removal from near-infrared imaging spectroscopy data of the Moon. *Journal of Geophysical Research: Planets*, *116*(E6).

1267 Daubar, I. J., Kring, D. A., Swindle, T. D., Jull, A. J. T. (2002). Northwest Africa
1268 482: A crystalline impact-melt breccia from the lunar highlands. *Meteoritics &*
1269 *Planetary Science*, *37*, 1797–1813, doi:10.1111/j.1945-5100.2002.tb01164.x.
1270
1271 Denevi, B. W., Koeber, S. D., Robinson, M. S., Garry, W. B., Hawke, B. R., Tran,
1272 T. N., Lawrence, S. J., Keszthelyi, L. P., Barnouin, O. S., Ernst, C. M.,
1273 Tornabene, L. L. (2012). Physical constraints on impact melt properties from
1274 Lunar Reconnaissance Orbiter Camera images. *Icarus*, *219*, 665–675,
1275 doi:10.1016/j.icarus.2012.03.020.
1276
1277 Dhingra, D., Pieters, C. M., Head, J. W., Isaacson, P. J. (2013). Large
1278 mineralogically distinct impact melt feature at Copernicus crater - Evidence for
1279 retention of compositional heterogeneity. *Geophysical Research Letters, 10,* 1-6,
1280 doi:10.1002/grl.50255.
1281
1282 Dong, C., Carter, L. M. (2014). Analysis and comparison of physical properties
1283 and morphology of impact melt flows on Venus and the Moon. *American*
1284 *Geophysical Union, Fall Meeting 2014*, Abstract P21B-3914.
1285

1286 Flemming, R.L. (2007) Micro X-ray diffraction (μXRD): a versatile technique for
1287 characterization of Earth and planetary materials. *Canadian Journal of Earth*
1288 *Sciences*, 44, 1333-1346, doi:10.1139/E07-020.
1289
1290 French, Bevan M. (1998) *Traces of catastrophe: A handbook of shock-*
1291 *metamorphic effects in terrestrial meteorite impact structures*. Lunar and
1292 Planetary Institute.
1293
1294 Fullagar, R., Torrence, R. (1991). Obsidian exploitation at Umleang, Lou Island.
1295 *Report of the Lapita Homeland Project*, *20*, 113-43.
1296
1297 Gaddis, L. R., Pieters, C. M., Hawke, B. R. (1985). Remote sensing of lunar
1298 pyroclastic mantling deposits. *Icarus*, *61*, 461–489, doi:10.1016/0019-
1299 1035(85)90136-8.
1300
1301 Glotch, T. D., Lucey, P. G., Bandfield, J. L., Greenhagen, B. T., Thomas, I. R.,
1302 Elphic, R. C., Bowles, N., Wyatt, M. B., Allen, C. C., Donaldson Hanna, K.,
1303 Paige, D. A. (2010). Highly Silicic Compositions on the Moon. *Science*, *329*,
1304 1510–1513, doi:10.1126/science.1192148.
1305

1306 Green, R. O., and 53 colleagues (2011). The Moon Mineralogy Mapper (M3)
1307 imaging spectrometer for lunar science: Instrument description, calibration, on-
1308 orbit measurements, science data calibration and on-orbit validation. *Journal of*
1309 *Geophysical Research*, *116*, doi:10.1029/2011JE003797.
1310
1311 Grieve, R. A. (1975). Petrology and chemistry of the impact melt at Mistastin
1312 Lake crater, Labrador. *Geological Society of America Bulletin*, *86*, 1617-1629.
1313
1314 Harmon, J. K., Nolan, M. C., Husmann, D. I., Campbell, B. A. (2012). Arecibo
1315 radar imagery of Mars: The major volcanic provinces. *Icarus*, *220*, 990–1030,
1316 doi:10.1016/j.icarus.2012.06.030.
1317
1318 Hawke, B.R., Head, J.W. (1977). Impact melt in lunar crater interiors. In: D.J.
1319 Roddy, R.O. Pepin, and R.B. Merrill (Eds.), Impact and explosion cratering.
1320 Pergamon Press, New York, NY, pp. 815.
1321
1322 Heather, D. J., Dunkin, S. K. (2003). Geology and stratigraphy of King crater,
1323 lunar farside. *Icarus*, *163*, 307–329, doi:10.1016/S0019-1035(02)00063-5.
1324
1325 Hill, R. J., Tsambourakis, G., Madsen, I. C. (1993). Improved petrological modal
1326 analyses from X-ray powder diffraction data by use of the Rietveld method I.

1327 Selected igneous, volcanic, and metamorphic rocks. *Journal of Petrology*, 34,
1328 867–900.
1329
1330 Hopkins, R. T., Tornabene, L. L., Osinski, G. R. (2017). The central uplift of
1331 Elorza Crater: Insights into its geology and possible relationships to the Valles
1332 Marineris and Tharsis regions. *Icarus*, *284*, 284-304.
1333
1334 Horgan, B. H. N., Cloutis, E. A., Mann, P., Bell, J. F. (2014). Near-infrared
1335 spectra of ferrous mineral mixtures and methods for their identification in
1336 planetary surface spectra. *Icarus*, *234*, 132–154, doi:10.1016/j.icarus.2014.02.031.
1337
1338 Howard, K.A., Wilshire, H.G. (1975). Flows of impact melt at lunar craters.
1339 *Journal of Research of the U.S. Geological Survey, 3*, 237.
1340
1341 Hui, H., Hess, K.-U., Zhang, Y., Nichols, A. R. L., Peslier, A. H., Lange, R. A.,
1342 Dingwell, D. B., Neal, C. R. (2018) Cooling rates of lunar orange glass beads.
1343 *Earth and Planetary Science Letters, 503*, 88-94.
1344
1345 Isaacson, P. J., Pieters, C. M., Besse, S., Clark, R. N., Head, J. W., Klima, R. L.,
1346 Mustard, J. F., Petro, N. E., Staid, M. I., Sunshine, J. M., Taylor, L. A., Thaisen,
1347 K. G., Tompkins, S. (2011). Remote compositional analysis of lunar olivine-rich

1348 lithologies with Moon Mineralogy Mapper (M3) spectra. *Journal of Geophysical*
1349 *Research*, *116*, E00G11, doi:10.1029/2010JE003731.
1350
1351 Kahraman, S., Toraman, O. Y., Cayirli, S. (2018). Predicting the strength and
1352 brittleness of rocks from a crushability index. *Bulletin of Engineering geology and*
1353 *the Environment*, *77*, 1639-1645.
1354
1355 Karson, J. A., Wysocki, R. (2012). Do-it-yourself lava flows: Science, art and
1356 education in the Syracuse University LavaProject. *Earth*, *57*, 38-41.
1357
1358 Keszthelyi, L., Denlinger, R. (1996). The initial cooling of pahoehoe flow lobes,
1359 *Bulletin of Volcanology*, *58*, 5–18, doi:10.1007/s004450050121.
1360
1361 Klima, R. L., Dyar, M. D., Pieters, C. M. (2011). Near-infrared spectra of
1362 clinopyroxenes: Effects of calcium content and crystal structure. *Meteoritics &*
1363 *Planetary Science*, *46*, 379–395, doi:10.1111/j.1945-5100.2010.01158.x.
1364
1365 Klug, H.P., Alexander, L.E. (1962). X-ray diffraction procedures, 3rd Edition.
1366 Wiley, New York, NY, pp. 716.
1367

1368 McEwen, A. S., Robinson, M. S., Eliason, E. M., Lucey, P. G., Duxbury, T. C.,
1369 Spudis, P. D. (1994). Clementine observations of the Aristarchus region of the
1370 Moon. *Science, 266*, 1858-1862, doi:10.1126/science.266.5192.1858.
1371
1372 Mader, M. M., Osinski, G. R. (2018). Impactites of the Mistastin Lake impact
1373 structure: Insights into impact ejecta emplacement. *Meteoritics & Planetary*
1374 *Science*, *53*, 2492-2518.
1375
1376 Morota, T., Haruyama, J., Miyamoto, H., Honda, C., Ohtake, M., Yokota, Y.,
1377 Matsunaga, T., Hirata, N., Demura, H., Takeda, H., Ogawa, Y., Kimura, J. (2009).
1378 Formation age of the lunar crater Giordano Bruno. *Meteoritics & Planetary*
1379 *Science*, *44*, 1115–1120, doi:10.1111/j.1945-5100.2009.tb01211.x.
1380
1381 Morrison, A. A., Zanetti, M., Hamilton, C. W., Lev, E., Neish, C. D., Whittington,
1382 A. G. (2019). Rheological investigation of lunar highland and mare impact melt
1383 simulants. *Icarus*, *317*, 307–323, doi:10.1016/j.icarus.2018.08.001.
1384
1385 Mustard, J. F., Pieters, C. M., Isaacson, P. J., Head, J. W., Besse, S., Clark, R. N.,
1386 Klima, R. L., Petro, N. E., Staid, M. I., Sunshine, J. M., Runyon, C. J., Tompkins,
1387 S. (2011). Compositional diversity and geologic insights of the Aristarchus crater

1388 from Moon Mineralogy Mapper data. *Journal of Geophysical Research*, *116*(E6),
1389 E00G12, doi:10.1029/2010JE003726.
1390
1391 Neish, C. D., Blewett, D. T., Bussey, D. B. J., Lawrence, S. J., Mechtley, M.,
1392 Thomson, B. J. (2011). The surficial nature of lunar swirls as revealed by the
1393 Mini-RF instrument. *Icarus*, *215*, 186-196.
1394
1395 Neish, C. D., Blewett, D. T., Harmon, J. K., Coman, E. I., Cahill, J. T. S., Ernst,
1396 C. M. (2013). A comparison of rayed craters on the Moon and Mercury. *Journal*
1397 *of Geophysical Research-Planets*, *118*, 2247–2261, doi:10.1002/jgre.20166.
1398
1399 Neish, C. D., Carter, L. M. (2014). Planetary radar. In *Encyclopedia of the Solar*
1400 *System* (pp. 1133-1159). Elsevier.
1401
1402
1403 Neish, C. D., Madden, J., Carter, L. M., Hawke, B. R., Giguere, T., Bray, V. J.,
1404 Osinski, G. R., Cahill, J. T. S. (2014). Global distribution of lunar impact melt
1405 flows, *Icarus*, *239*, 105–117, doi:10.1016/j.icarus.2014.05.049.
1406
1407 Neish, C. D., Hamilton, C. W., Hughes, S. S., Nawotniak, S. K., Garry, W. B.,
1408 Skok, J. R., Elphic, R. C., Schaefer, E., Carter, L. M., Bandfield, J. L., Osinski, G.

1409 R., Lim, D., Heldmann, J. L. (2017). Terrestrial analogues for lunar impact melt
1410 flows. *Icarus*, *281*, 73–89, doi:10.1016/j.icarus.2016.08.008.
1411
1412 Nozette, S., Spudis, P., Bussey, B., Jensen, R., Raney, K., Winters, H.,
1413 Lichtenberg, C.L., Marinelli, W., Crusan, J., Gates, M., and Robinson, M. (2010).
1414 The Lunar Reconnaissance Orbiter Miniature Radio Frequency (Mini-RF)
1415 Technology Demonstration, *Space Science Reviews*, *150*, 285–302,
1416 doi:10.1007/s11214-009-9607-5.
1417
1418 Osinski, G. R., Tornabene, L. L., Grieve, R. A. F. (2011). Impact ejecta
1419 emplacement on terrestrial planets, *Earth and Planetary Science Letters*, *310*,
1420 167–181, doi:10.1016/j.epsl.2011.08.012.
1421
1422 Osinski, G. R., Grieve, R. A. F., Bleacher, J. E., Neish, C. D., Pilles, E. A.,
1423 Tornabene, L. L. (2018). Igneous rocks formed by hypervelocity impact. *Journal*
1424 *of Volcanology and Geothermal Research*, *353*, 25–54,
1425 doi:10.1016/j.jvolgeores.2018.01.015.
1426
1427 Pieters, C. M. (1983). Strength of mineral absorption features in the transmitted
1428 component of near-infrared reflected light: First results from RELAB. *Journal of*
1429 *Geophysical Research: Solid Earth*, *88*, 9534-9544.

Pieters, C., and 19 colleagues (2009). The Moon Mineralogy Mapper (M^3) on Chandrayaan-1. *Current Science,96*, 500-505.

Plescia, J. B., Robinson, M. S., Paige, D. A. (2010). Giordano Bruno: The Young and the Restless. *Lunar and Planetary Institute Science Conference Abstracts*, *41*, 2038.

Robinson, M.S., and 22 colleagues (2010). Lunar Reconnaissance Orbiter Camera (LROC) instrument overview, *Space Science Reviews, 150*, 81-124, doi:10.1007/s11214-010-9634-2.

Ryder, G., Norman, M. D. (1980). Catalog of Apollo 16 Rocks, NASA Curatorial Branch Publication 52. *NASA/Johnson Space Center, Houston*.

Simonds, C.H., Warner, J.L., Phinney, W.C. (1976). Thermal regimes in cratered terrain with emphasis on the role of impact melt, *American Mineralogist, 61*, 569–577.

1449 Smrekar, S., Pieters, C. M. (1985). Near-infrared spectroscopy of probable impact
1450 melt from three large lunar highland craters, *Icarus, 63*, 442–452,
1451 doi:10.1016/0019-1035(85)90056-9.
1452
1453 Stopar, J. D., Hawke, B. R., Robinson, M. S., Denevi, B. W., Giguere, T. A.,
1454 Koeber, S. D. (2014). Occurrence and mechanisms of impact melt emplacement
1455 at small lunar craters, *Icarus*, *243*, 337–357, doi:10.1016/j.icarus.2014.08.011.
1456
1457 Sutton, S. R., Karner, J., Papike, J., Delaney, J. S., Shearer, C., Newville, M.,
1458 Eng, P., Rivers, M., Dyar, M. D. (2005). Vanadium K edge XANES of synthetic
1459 and natural basaltic glasses and application to microscale oxygen barometry.
1460 *Geochimica Et Cosmochimica Acta*, *69*, 2333–2348,
1461 doi:10.1016/j.gca.2004.10.013.
1462
1463 Taylor, R. S., McLennan, S. (2009). Planetary crusts: Their composition, origin
1464 and evolution. Cambridge University Press, Cambridge, UK, pp. 378.
1465
1466 Timms, N.E., Erickson, T.M., Pearce, M.A., Cavosie, A.J., Schmieder, M.,
1467 Tohver, E., Reddy, S.M., Zanetti, M.R., Nemchin, A.A., Wittmann, A. (2017). A
1468 pressure-temperature phase diagram for zircon at extreme conditions. *Earth-*
1469 *Science Reviews*, *165*, 185-202.

1470

1471 Tompkins, S., Pieters, C. M. (2010). Spectral characteristics of lunar impact melts
1472 and inferred mineralogy. *Meteoritics & Planetary Science*, *45*, 1152–1169,
1473 doi:10.1111/j.1945-5100.2010.01074.x.

1474

1475 Vaughan, W. M., Head, J. W., Wilson, L., Hess, P. C. (2013). Geology and
1476 petrology of enormous volumes of impact melt on the Moon: A case study of the
1477 Orientale basin impact melt sea. *Icarus*, *223*, 749-765,
1478 doi:10.1016/j.icarus.2013.01.017.

1479

1480 Wānke, H., Palme, H., Baddenhausen H., Dreibus, G., Jagoutz, E., Kruse, H.,
1481 Palme, C., Spettel, B., Teschke, F., Thacker, R. (1975) New data on the chemistry
1482 of lunar samples: Primary matter in the lunar highlands and the bulk composition
1483 of the moon. *Proc. Lunar Sci. Conf., 6,* 1313-1340.

1484

1485 Yamamoto, S., Nakamura, R., Matsunaga, T., Ogawa, Y., Ishihara, Y., Morota,
1486 T., Hirata, N., Ohtake, M., Hiroi, T., Yokota, Y., Haruyama, J. (2010). Possible
1487 mantle origin of olivine around lunar impact basins detected by SELENE. *Nature*
1488 *Geoscience*, *3*, 533, doi:10.1038/ngeo897.

1489

1490 Zanetti, M., Hiesinger, H., van der Bogert, C. H., Jolliff, B. L. (2011).
1491 Observation of Stratified Ejecta Blocks at Aristarchus Crater. *Lunar and*
1492 *Planetary Science Conference*, *42*, 2262.
1493
1494 Zanetti, M. R. (2015). Investigating the Complexity of Impact Crater Ejecta. *Arts*
1495 *& Sciences Electronic Theses and Dissertations, Washington University in St.*
1496 *Louis*, 694.
1497
1498 Zhang, J., Jolliff, B. L. (2008). Aristarchus Region: A Potential Location for
1499 Future Surface Exploration. *Lunar and Planetary Institute Science Conference*
1500 *Abstracts, 34,* 2534.
1501
1502 Zisk, S. H., Hodges, C. A., Moore, H. J., Shorthill, R. W., Thompson, T. W.,
1503 Whitaker, E. A., Wilhelms, D. E. (1977). The Aristarchus-Harbinger region of the
1504 moon: Surface geology and history from recent remote-sensing observations. *The*
1505 *Moon*, *17*, 59–99, doi:10.1007/BF00566853.